Two-layer baroclinic eddy heat fluxes: zonal flows and energy balance

Andrew F. Thompson[1] & William R. Young

December 12, 2006

Scripps Institution of Oceanography
University of California, San Diego
La Jolla, CA 92093-0213

[1]Corresponding author current address:
School of Environmental Sciences
University of East Anglia
Norwich NR4 7TJ, U.K.
Andrew.F.Thompson@uea.ac.uk

Abstract

The eddy heat flux generated by statistically equilibrated baroclinic turbulence supported on a uniform, horizontal temperature gradient is examined using a two-layer β-plane quasigeostrophic model. The dependence of the eddy diffusivity of temperature, D_τ, on external parameters such as β, bottom friction κ, the deformation radius λ and the velocity jump $2U$ is provided by numerical simulations at 110 different points in the parameter space $\beta_* = \beta\lambda^2/U$ and $\kappa_* = \kappa\lambda/U$. There is a special "pivot" value of β_*, $\beta_*^{\mathrm{piv}} \approx 11/16$, at which D_τ depends weakly on κ_*. But otherwise D_τ has a complicated dependence on both β_* and κ_*, highlighted by the fact that reducing κ_* leads to increases (decreases) in D_τ if β is less than (greater than) β_*^{piv}. Existing heat-flux parameterizations, based on Kolmogorovian cascade theories, predict that D_τ is nonzero and independent of κ_* in the limit $\kappa_* \to 0$. Our simulations show indications of this regime provided that $\kappa_* \leq 0.04$ and $0.25 \leq \beta_* \leq 0.5$.

All important length scales in this problem, namely the mixing length, the scale of the energy containing eddies, the Rhines scale and the spacing of the zonal jets, converge to a common value as bottom friction is reduced. The mixing length and jet spacing do not decouple in the parameter regime considered here, as predicted by

cascade theories. The convergence of these length scales is due to the formation of jet-scale eddies that align along the eastward jets. The baroclinic component of these eddies helps force the zonal mean flow, which occurs through non-zero Reynolds stress correlations in the upper layer, as opposed to the barotropic mode. This behavior suggests that the dynamics of the inverse barotropic cascade is insufficient to fully describe baroclinic turbulence.

1 Introduction

Rhines (1977) and Salmon (1980) characterize energy transfers in baroclinic turbulence as a direct cascade of the baroclinic mode and a simultaneous inverse cascade of the barotropic mode. This dual cascade-scenario serves as an interpretive framework for recent parameterizations of meridional eddy heat and potential vorticity fluxes (Larichev & Held 1995, Held & Larichev 1996, Lapeyre & Held 2003). In these theories the barotropic inverse cascade proceeds to small wavenumbers till the cascade halts at a wavenumber k_0. The length k_0^{-1} characterizes the largest barotropic eddies and k_0^{-1} is also the mixing length of heat and potential vorticity. There are two mechanisms which might determine k_0 by slowing or halting the inverse cascade: the planetary potential vorticity (PV) gradient, β, and bottom friction.

Because the β-effect does not dissipate energy, β alone cannot halt the inverse cascade and determine k_0. Thus bottom drag plays an essential role at the terminus of the inverse cascade by dissipating the kinetic energy continually supplied by release of available potential energy. In other words, truly halting the inverse cascade requires dissipation at large scales, and only bottom drag can accomplish this. An extreme case that makes this point is the problem of statistically steady baroclinic turbulence with $\beta = 0$. At this $\beta = 0$ end-point, the eddy heat flux is exponentially sensitive to the strength of the bottom drag coefficient (Thompson & Young 2006).

In view of the importance of bottom drag, it is dismaying that the bottom drag coefficient does not play an explicit role in the heat-flux parametrizations proposed by Held & Larichev (1996) and Lapeyre & Held (2003, LH03 hereafter). A defense of these dragless heat-flux parameterizations relies on the ability of β to direct energy into zonal flows (Rhines 1975, Williams 1979, Panetta 1993, Vallis & Maltrud 1993, Lee 1997). Zonal flows do not contribute to meridional eddy diffusion and therefore do not release available potential energy. In this view the strong zonal flows spontaneously generated by baroclinic turbulence, see Figures 1 and 2, serve as a non-diffusive reservoir of barotropic kinetic energy and, through bottom friction, as the energy sink at the terminal wavenumber of the inverse cascade (Smith *et al.* 2002). Thus it is possible to maintain, following LH03, that with $\beta \neq 0$ the amplitude of eddy heat fluxes is insensitive to the bottom drag coefficient.

This seems too good to be true, and throughout most of the parameter space it is: a main goal in this computational study of baroclinic instability is to document the importance of bottom drag in limiting baroclinic eddy heat fluxes. We consider the combined effects of β and bottom friction on meridional eddy heat fluxes and report results based on a suite of 110 statistically equilibrated simulations of baroclinic turbulence. These simulations significantly extend and augment the parameter regimes of previous studies. Although the dependence on bottom drag is not nearly as strong as the exponential relation found by Thompson & Young (2006) in the $\beta = 0$ limit, the new simulations show that even with substantial β, bottom drag remains an important control parameter.

In section **2** we introduce the energy balance integral and define the eddy diffusivities that are used to summarize the suite of simulations. In section **3** we review and assess the LH03 theory of baroclinic eddy fluxes. In section **4** we survey the important length scales in the problem (the mixing length, the scale of the energy containing eddies, the Rhines scale, the spacing of the zonal jets) and show that when the bottom drag is sufficiently weak, all length scales converge to a common value. We also show that large, jet-scale eddies make the dominant contribution to the eddy heat flux and force the zonal mean flow through upper-layer (not barotropic) Reynolds stresses. In section **5** we confirm that eddy diffusivities and heat fluxes are insensitive to the domain scale L, and to the hyperdiffusivity. Our conclusions are presented in section **6**. The equations of motion are summarized in appendix **A**.

2 Eddy fluxes and diffusivities

To summarize the results of our simulations, we calculate an eddy diffusivity of temperature, D_τ, and obtain the dependence of D_τ on external parameters such as the domain size L, the bottom drag coefficient κ, the Rossby deformation radius λ, the imposed velocity jump $2U$ and β. Our notation is introduced systematically in Appendix **A** and is largely the same as that of Larichev & Held (1995): $\tau(x, y, t)$ and $\psi(x, y, t)$ are the disturbance stream functions of the baroclinic and barotropic modes respectively. The baroclinic stream function τ plays the role of an interface displacement or a thermal field. The large scale gradient of the baroclinic mode is $-U$, and thus a precise definition of the eddy diffusivity of temperature, D_τ, is

$$D_\tau \equiv U^{-1}\langle \psi_x \tau \rangle \,. \tag{1}$$

Here $\langle\rangle$ denotes both a horizontal average over the square $2\pi L \times 2\pi L$ domain, and an additional time average to remove residual turbulent fluctuations. An important point is that D_τ is useful only if it is insensitive to the domain size L (Haidvogel & Held 1980). In this case one can hope that D_τ inferred from a spatially homogeneous calculation can be employed in a more realistic flow with scale separation between a slowly varying mean and baroclinic eddies (Pavan & Held 1996).

The quantity $\langle\psi_x\tau\rangle$ in (1) is the product of the barotropic meridional velocity, ψ_x, and the thermal field τ i.e., the meridional heat flux is proportional to $\langle\psi_x\tau\rangle$. Moreover, the mechanical energy balance in a statistically steady state (see Appendix **A**) is

$$U\lambda^{-2}\left\langle\psi_x\tau\right\rangle = \kappa\left\langle|\boldsymbol{\nabla}\psi - \sqrt{2}\boldsymbol{\nabla}\tau|^2\right\rangle + hyp\nu\,, \tag{2}$$

where "*hypν*" indicates the hyperviscous dissipation of energy. The first term on the right hand side of (2) is the mechanical energy dissipation (Watts per kilogram) by bottom drag, κ. We will refer to dissipation by bottom friction as

$$\varepsilon \equiv \kappa\left\langle|\boldsymbol{\nabla}\psi - \sqrt{2}\boldsymbol{\nabla}\tau|^2\right\rangle\,, \tag{3}$$

which neglects the hyperviscous contribution in (2). The left hand side of (2) is the energy extracted from the unstable horizontal temperature gradient by baroclinic instability. Enstrophy budgets also identify $\langle\psi_x\tau\rangle$ as the large-scale source balancing the hyperviscous enstrophy sink at high wavenumbers.

As an alternative to the baroclinic-barotropic decomposition, the system can be represented in terms of two layers; the layerwise velocities and potential vorticities are defined in terms of ψ and τ in Appendix **A**. The domain-averaged PV fluxes in the upper and lower layers are linearly related to the eddy heat flux by the Taylor-Bretherton relationship

$$-\langle v_1 q_1\rangle = \langle v_2 q_2\rangle = \lambda^{-2}\langle \psi_x \tau\rangle \ . \tag{4}$$

The basic state gradients of upper and lower layer PV are $\beta + U\lambda^{-2}$ and $\beta - U\lambda^{-2}$ respectively. Thus the upper ($n = 1$) and lower ($n = 2$) layer PV diffusivities are related to D_τ by

$$\begin{aligned} D_\tau &= D_1\left(1+\frac{\beta\lambda^2}{U}\right), & (5)\\ D_\tau &= D_2\left(1-\frac{\beta\lambda^2}{U}\right). & (6)\end{aligned}$$

Thus a single quantity, conveniently defined as D_τ in (1), summarizes all of the important quadratic power integrals and fluxes in homogeneous baroclinic turbulence.

Dimensional considerations (Haidvogel & Held 1980) show that

$$D_\tau = U\lambda \times D_{\tau *}\left(\frac{L}{\lambda}, \frac{\kappa\lambda}{U}, \frac{\beta\lambda^2}{U}, \frac{\nu}{UL^7}\right) , \tag{7}$$

where $D_{\tau *}$ is a dimensionless function. The final argument of $D_{\tau *}$, involving the hyperviscosity ν, is relatively small (see section **5**). For brevity we suppress reference to this hyperviscous parameter. We also focus on a single value $L/\lambda = 25$, however, we check for dependence on L as described in section **5**.

Figure 3(a) summarizes a suite of 110 numerical simulations revealing the main features of the function $D_{\tau *}(25, \beta_*, \kappa_*)$, where $\beta_* \equiv \beta\lambda^2/U$ and

$\kappa_* \equiv \kappa\lambda/U$. $D_{\tau *}$ varies over five orders of magnitude in response to much smaller changes in β_* and κ_*. Some trends in Figure 3 are clear: $D_{\tau *}$ decreases monotonically with increasing β_*. However, other dependences are more complicated, particularly those related to bottom drag. Close to the special "pivot" value $\beta_* = \beta_*^{\mathrm{piv}} \approx 11/16$, $D_{\tau *}$ has a weak dependence on bottom friction. For $\beta_* < \beta_*^{\mathrm{piv}}$, increasing bottom friction reduces $D_{\tau *}$, whereas for $\beta_* > \beta_*^{\mathrm{piv}}$, increasing bottom friction increases $D_{\tau *}$. This behavior is shown in Figure 3(*b*) which illustrates the κ_*-variation of D_τ at five values of β_*. The same trends are evident in Figure 14 of Panetta (1993).

Thompson & Young (2006) discuss the limiting case $\beta_* = 0$ in detail. Their conclusion is that a well-defined D_τ — independent of domain size — exists provided that κ_* is not too small. The $\beta_* = 0$ points in Figure 3 satisfy this condition and are in Thompson & Young's local mixing regime. However this constraint means that the weakly damped runs with $\kappa_* \leq 0.08$ cannot be extended to values of β less than about 0.25: to go below $\beta = 0.25$ and $\kappa_* = 0.08$ requires increasing the domain size so the largest eddies are smaller than the domain.

Notice that Figure 3 shows non-zero diffusivities when $\beta_* \geq 1$. This is because bottom friction destabilizes the system beyond the frictionless critical value $\beta_* = 1$ (Holopainen 1961; Pedlosky 1987; Arbic & Flierl 2004).

Consequently statistically steady, small non-zero values of D_τ are achievable out to at least $\beta_* \approx 1.5$.

To summarize the results in Figure 3 it is useful to have a compact formula for $D_{\tau *}$ in terms of β_* and κ_*. The empirical formula

$$D_{\tau *} \approx \beta_*^{-4} \left[1.7 + (3 - 4\beta_*)\,\kappa_*\right]^{-4} \,, \quad \text{provided } 0.25 \leq \beta_* \leq 1.25 \,, \qquad (8)$$

fits $D_{\tau *}$ to within ±10% over a broad range of β_* and κ_* values (see Figure 4). The dotted curve in Figure 3 is $D_{\tau *} \approx 0.12\beta_*^{-4}$ which is obtained from (8) by setting $\kappa_* = 0$. The fit (8) still has the problem that $D_{\tau *}$ grows to infinity as $\beta_* \to 0$. At small values of β_* a different expression, tending towards the exponential dependence on κ_* observed by Thompson & Young (2006), is required.

3 Review and Assessment of LH03

The energy balance in (2) provides one relationship between the dissipation ε and the energy production, or equivalently, the eddy diffusivity D_τ. Specifically, using the definitions of D_τ and ε in (1) and (3), and neglecting the hyperviscous dissipation, we obtain

$$\frac{U^2}{\lambda^2} D_\tau \approx \varepsilon \,. \qquad (9)$$

Figure 5(*a*) shows that (9) is an excellent approximation; the small deviation of the ratio $\varepsilon\lambda^2/U^2D_\tau$ from 1 is due to the *hypν* contribution to the dissipation. The hyperviscous dissipation is never more than 12% and can be reduced further by increasing the resolution (see section **5**).

Held & Larichev (1996) propose a closure obtained from cascade arguments in which β halts the barotropic inverse cascade by directing energy into zonal modes. Forming a diffusivity from β and the inverse cascade rate (which is assumed to be equivalent to ε in a steady state), dimensional analysis gives $D_\tau = c\varepsilon^{3/5}\beta^{-4/5}$, where c is a dimensionless constant. This relation between D, ε and β is supported by the arguments and numerical simulations of Smith *et al.* (2002), which employ a barotropic model. Combining $D_\tau = c\varepsilon^{3/5}\beta^{-4/5}$ with (9) gives the Held & Larichev (1996) result, namely $D_\tau = c^{5/2}U^3/(\lambda^3\beta^2)$.

3.1 Selection of the lower-layer diffusivity

An immediate problem is that there are three diffusivities: in addition to D_τ we have the PV diffusivities D_1 and D_2 in (5) and (6). If one of these three diffusivities involves only ε and β, then the other two will have additional dependence on other parameters. Thus the association of the dimensional combination $c\varepsilon^{3/5}\beta^{-4/5}$ with D_τ, as opposed to D_1 or D_2, is a significant hypothesis. Indeed, LH03 updated the theory of Held & Larichev (1996) by identifying the eddy diffusivity $c\varepsilon^{3/5}\beta^{-4/5}$ with the lower layer PV diffusivity D_2, rather than D_τ:

$$D_2 \approx c\varepsilon^{3/5}\beta^{-4/5} . \tag{10}$$

The motivation for (10) is that the weaker PV gradient in the lower layer allows larger meridional particle excursions so that lower layer PV behaves more like a passive tracer. The ratio $\beta^{-4/5}\epsilon^{3/5}D_2^{-1}$ is shown in Figure 5(b) and there is strong and systematic dependence on both β and κ. However the ratio is almost constant for the runs with $0.25 \le \beta_* \le 0.5$ and $\kappa_* \le 0.08$ and it is in this corner of the parameter space that the theoretical arguments of LH03 might apply. This region is discussed in greater detail below.

Using (6) and (9), D_2 and ε are eliminated from (10), which yields the main prediction of LH03

$$D_\tau/U\lambda \approx c^{5/2}\beta_*^{-2}\left(1-\beta_*\right)^{5/2} , \tag{11}$$

where $\beta_* \equiv \beta\lambda^2/U$. The relation above[1] is the dashed curve in Figure 3 with $c = 1.65$.

---

[1] LH03 used $c = 1.25$ to fit their numerical results at $\kappa_* = 0.16$. We use a larger value $c = 1.65$ to match our more weakly damped simulations with $\kappa_* \le 0.08$.

3.2 The rampant barotropic mode

An important assumption in the LH03 heat-flux closure (invoked implicitly in the paragraphs above) is that the barotropic mode is rampant. Specifically, LH03 assumes that the inverse cascade rate of the *barotropic* mode,

$$\varepsilon_\psi \equiv \kappa \langle |\boldsymbol{\nabla}\psi|^2 \rangle \,, \tag{12}$$

is nearly equal to the total cascade rate ε defined in (3). This assumption is used to construct (10) and is motivated by the results of Smith *et al.* (2002). These authors conducted a series of barotropic simulations with random small scale forcing and dissipation via linear bottom drag. Smith *et al.* showed that in the β-dominated regime of barotropic turbulence, the meridional eddy diffusivity is proportional to $\varepsilon_\psi^{3/5}\beta^{-4/5}$, where ε_ψ is the energy supplied by the random small-scale forcing.

A logical application of the results of Smith *et al.* to the baroclinic problem begins by writing the barotropic mode equation (42) in the form

$$\zeta_t + J(\psi, \zeta) + \beta\psi_x = f_\psi - \kappa\zeta - \nu\nabla^8\zeta \,, \tag{13}$$

where $\zeta \equiv \nabla^2\psi$, and the forcing of the barotropic mode by the baroclinic mode is

$$f_\psi \equiv \sqrt{2}\kappa\nabla^2\tau - U\nabla^2\tau_x - J(\tau, \nabla^2\tau) \,. \tag{14}$$

The barotropic energy equation is formed by multiplying (13) by ψ and averaging. We then find that the energy supplied to the barotropic inverse cascade is $\langle \psi f_\psi \rangle$ and that the dissipation of barotropic energy is ε_ψ in (12) (neglecting hyperviscous contributions). The assumption is that the theory and simulations of Smith *et al.* (2002) identify a universal scaling regime of barotropic turbulence in which almost[2] all important physical quantities are determined by dimensional analysis based on only β and the cascade rate $\varepsilon_\psi \approx \langle \psi f_\psi \rangle$. In other words, all other details of the barotropic forcing are irrelevant. Thus in consistently applying the results of Smith *et al.* (2002) to the baroclinic problem one should use ε_ψ, rather than ε, in scaling relations such as (10); consequently (11) cannot be correct unless

$$\varepsilon \approx \varepsilon_\psi \, . \tag{15}$$

Figure 6 shows that (15) is not true in general and that the ratio $\varepsilon_\psi/\varepsilon$ is a function of both β_* and κ_*. It is striking that throughout much of the parameter space $\varepsilon_\psi/\varepsilon$ in Figure 6 is significantly larger than one. This is expected because bottom drag retards the lower-layer flow so that estimates of the dissipation using the barotropic velocity are too large (Arbic & Flierl 2004). The sensitivity of $\varepsilon_\psi/\varepsilon$ is notable, and one can further explain this by

---

[2] For discussion of “almost” see subsection 3.4.

expanding ε in (3) as

$$\varepsilon = \varepsilon_\psi + \kappa \left(-2\sqrt{2}\langle \boldsymbol{\nabla}\psi \boldsymbol{\cdot} \boldsymbol{\nabla}\tau \rangle + 2\langle |\boldsymbol{\nabla}\tau|^2 \rangle \right) . \tag{16}$$

The second term on the right hand side of (16) is negative because there is a strong anti-correlation between τ and $\zeta \equiv \nabla^2\psi$:

$$-2\sqrt{2}\langle \boldsymbol{\nabla}\psi \boldsymbol{\cdot} \boldsymbol{\nabla}\tau \rangle = 2\sqrt{2}\langle \zeta\tau \rangle < 0 \,, \tag{17}$$

(see Figure 7). This anti-correlation means that ε can be significantly less than the barotropic cascade rate ε_ψ.

3.3 Conditions for validity of LH03

Because of the approximation (15) the theory of LH03 cannot apply across the entire parameter space shown in Figure 3: in most of the parameter space the flow is significantly baroclinic in the sense that $\varepsilon_\psi/\varepsilon \gtrsim 2$. To isolate a corner of parameter space in which the parameterization (11) might apply we limit attention to 15 runs with

$$0.02 \le \kappa_* \le 0.08 \,, \qquad \text{and} \qquad 0.25 \le \beta_* \le 0.5 \,. \tag{18}$$

The open symbols in Figure 8 show that at $\kappa_* = 0.02$ the approximation (15) is satisfied at the 10 to 20% level. Figure 9 shows some details of the run with $\beta_* = 0.25$ and $\kappa_* = 0.04$; the zonal mean velocity in panel (a) is strikingly barotropic. Comparing Figure 9(c) with the Hovmoller diagrams in panels (c) and (e) of Figure 1 shows that the zonal mean is more variable e.g., in Figure 9(c) the zonal jets meander across a considerable fraction of the domain.

Figure 10 shows some further details of these 15 runs. Figure 10(a) shows the diffusivity $D_{\tau *}$, and as suggested by LH03 $D_{\tau *}$ is insensitive to κ_*; this is particularly evident for the two most weakly damped runs with $\kappa_* = 0.02$ and 0.04. The remaining panels of Figure 10 show the barotropic eddy velocity

$$V \equiv \sqrt{\langle \psi_x'^2 \rangle}\,, \tag{19}$$

the mixing length

$$\ell_{\text{mix}} \equiv U^{-1} \sqrt{\left\langle \tau'^2 \right\rangle}\,, \tag{20}$$

and the correlation between ψ_x' and τ'

$$c_\tau \equiv \frac{D_\tau}{\ell_{\text{mix}} V}\,. \tag{21}$$

These three statistics have a greater individual sensitivity to κ_* than does their product D_τ. This is not in accord with LH03, which suggests that all three quantities should be independent of κ_*. The main puzzle here is that the κ-dependence of the correlation c_τ is opposite to that of the $\ell_{\text{mix}} V$. As κ_* is reduced both V and ℓ_{mix} increase while c_τ decreases so that D_τ is relatively constant. This behavior is suggestive of a large-scale baroclinic wave whose amplitude increases as κ decreases. We discuss this further in subsection 4.2.

3.4 The zonal mean flow

As explained above, a main assumption of LH03 is that forced-dissipative barotropic turbulence identifies a universal scaling regime in which almost all important statistical quantities, such as D, V, c_τ and ℓ_{mix} are determined by dimensional analysis based on only β and the cascade rate $\varepsilon_\psi \approx \langle \psi f_\psi \rangle$. However, since κ appears on the right hand side of the approximate energy balance[3]

$$\frac{U^2}{\lambda^2} D_\tau \approx \kappa \langle |\boldsymbol{\nabla} \psi|^2 \rangle \,, \tag{22}$$

there must be some component of the barotropic velocity varying as $\kappa^{-1/2}$ in order to balance the κ-independent energy generation on the left hand side.

In the view of Smith *et al.* (2002) and LH03 this dissipation is provided by

$$u_{\mathrm{J}} \equiv \sqrt{\langle \bar{\psi}_y^2 \rangle} \,, \tag{23}$$

where $\bar{\psi}(y,t)$ is the zonally averaged zonal velocity. Thus, assuming rough isotropy of the barotropic eddy components, the barotropic dissipation on

---

[3] We are making the LH03 approximation $\varepsilon \approx \varepsilon_\psi$ throughout this subsection so that (22) follows from (9).

the right hand side of (22) can be estimated as $\kappa\langle|\boldsymbol{\nabla}\psi|^2\rangle \approx \kappa u_{\mathrm{J}}^2 + 2\kappa V^2$. But since V is independent of κ in the LH03 limit, the energy balance (22) collapses to

$$\frac{U^2}{\lambda^2} D_\tau \approx \kappa u_{\mathrm{J}}^2 \,. \tag{24}$$

The closed symbols in Figure 8 show that (24) is valid at the 10 to 20% level for the runs with $\kappa_* = 0.02$.

The other important quantity associated with the zonal jets is distance between the eastward maxima, which we write as $2\pi\ell_{\mathrm{J}}$. If n_{J} is the number of jets (e.g., $n_{\mathrm{J}} = 5$ in Figure 1(a) and $n_{\mathrm{J}} = 2$ in Figure 9(a)) then

$$\ell_{\mathrm{J}} = \frac{L}{n_{\mathrm{J}}} \,. \tag{25}$$

Following Smith *et al.* (2002), ℓ_{J} is related to the other variables by arguing that the curvature $\bar{u}_{yy}$ is of order β:

$$u_{\mathrm{J}} \approx \alpha_{\mathrm{J}} \beta \ell_{\mathrm{J}}^2 \,, \tag{26}$$

where α_{J} is a dimensionless constant of order unity. Eliminating u_{J} between (24) and (26) one has

$$\ell_{\mathrm{J}} \approx \sqrt{\frac{U}{\alpha_{\mathrm{J}}\beta\lambda}} \left(\frac{D_\tau}{\kappa}\right)^{1/4} \propto \kappa_*^{-1/4} \,. \tag{27}$$

Thus these scaling arguments predict asymptotic decoupling between ℓ_{mix} and ℓ_{J} as $\kappa_* \to 0$: ℓ_{mix} is independent of κ_* while $\ell_{\mathrm{J}} \sim \kappa_*^{-1/4}$ so that $\ell_{\mathrm{J}} \gg \ell_{\mathrm{mix}}$.

The considerations above leads to an uncomfortable conclusion: according to (26) and (27) the shear in the zonal jets is of order

$$\frac{u_\mathrm{J}}{\ell_\mathrm{J}} \approx \alpha_\mathrm{J} \beta \ell_\mathrm{J} \propto \kappa_*^{-1/4}\,, \quad \text{as } \kappa_* \to 0. \tag{28}$$

Thus the zonal shear $\bar{u}_y$ is asymptotically faster than the turnover rate of the eddies[4]. According to this scale analysis the barotropic eddy component is strongly sheared by the zonal flow and cannot be regarded as isotropic, and this is inconsistent with the initial assumptions of the theory.

To rescue the theory from this inconsistency one can abandon (26) and (27) and instead use the assumption that the zonal shear scales with the eddy turnover rate:

$$\frac{u_\mathrm{J}}{\ell_\mathrm{J}} \approx \alpha_\mathrm{J} \left(\varepsilon \beta^2\right)^{1/5}\,. \tag{29}$$

The physical assumption is that there is a balance between the rate at which the zonal shear flow creates anisotropy and the eddy-eddy interactions which restore isotropy. Because of this dynamic balance the zonal flow cannot be regarded as a totally passive reservoir for excess kinetic energy. Eliminating u_J between (29) and (24) one obtains

$$\ell_\mathrm{J} \approx \frac{1}{\alpha_\mathrm{J} \beta^{2/5} \sqrt{\kappa}} \left(\frac{U^2}{\lambda^2} D_\tau \right)^{3/10} \propto \kappa_*^{-1/2}\,. \tag{30}$$

---

[4] Using dimensional analysis the eddy turnover rate is $(\varepsilon\beta^2)^{1/5}$, independent of κ_*.

Comparing (30) with (27) we see that ℓ_{J} now decouples even more strongly from ℓ_{mix} as $\kappa_* \to 0$.

3.5 Summary

We end this section by summarizing our conclusions regarding the LH03 parametrization (11) and the physical arguments underlying it. We have located a parameter range in which the flow is almost barotropic and strongly zonal in the sense that (24) is roughly satisfied at $\kappa_* = 0.02$. In this regime with $\kappa_* \ll 1$, D_τ is insensitive to variations of κ_* and, with adjustment of the constant c, (11) is close to the D_τ-data. These results are consistent with LH03 but are not totally persuasive. In addition to D_τ, the LH03 theory predicts that V, ℓ_{mix} and c_τ also depend weakly on κ_*. The simulations show an uncomfortable variation of these three quantities as κ_* is reduced; it is striking that the small changes in $D_\tau = c_\tau \ell_{\mathrm{mix}} V$ result from systematic changes[5] in c_τ that cancel those in $V\ell_{\mathrm{mix}}$.

The theory also makes the prediction that u_{J} and ℓ_{J} both increase as κ_* decreases. The variation of ℓ_{J} with κ_* is given by either (27) or (30), depending on whether one prefers (26) or (29). But in either case the pre-

---

[5] These variations in c_τ are characteristic of the whole parameter space, not just the corner shown in Figure 10.

diction is that $\ell_{\rm J}$ should be much larger than $\ell_{\rm mix}$. We discuss this point in section 4 where a main conclusion is that in fact $\ell_{\rm J} \approx \ell_{\rm mix}$. Because of these inconsistencies we conclude that the hypothetical regime underlying the parameterization (11) is not realized in the portion of parameter space surveyed in Figure 3. Further pursuit of this regime requires smaller κ_* and larger domains.

4 Length scales and eddy-mean interactions

4.1 Five length scales

The ε-β dimensional analysis of LH03 identifies

$$\ell_{\rm LH} \equiv \varepsilon^{1/5}\beta^{-3/5} \tag{31}$$

as the length scale of the large energetic barotropic eddies (see also Vallis & Maltrud 1993). This energy-containing length can be independently diagnosed as

$$\ell_0 \equiv \sqrt{\frac{\langle \psi'^2 \rangle}{\langle |\nabla\psi'|^2 \rangle}} \, . \tag{32}$$

The length scales $\ell_{\rm LH}$, ℓ_0 and $\ell_{\rm mix}$ (20) should be equivalent differing only by dimensionless factors of order unity. These three lengths should coincide with the halting scale of the inverse cascade.

Panetta (1993) suggests that ℓ_{J} in (25) can be related to the Rhines length ℓ_{R} diagnosed as

$$\ell_{\mathrm{R}} \equiv \sqrt{\mathcal{V}/\beta}\,, \tag{33}$$

where $\mathcal{V}$ is the square root of the total eddy kinetic energy[6],

$$\mathcal{V} \equiv \sqrt{\langle|\nabla\psi'|^2\rangle + \langle|\nabla\tau'|^2\rangle}\,. \tag{34}$$

Panetta (1993) argues that the jet spacing ℓ_{J} is well-predicted by (33) and we confirm this with our larger and higher resolution data set (see Thompson 2006 for details).

Figure 11 shows the five length scales ℓ_{mix}, $2\ell_{\mathrm{LH}}$, ℓ_0, ℓ_{R} and $\ell_{\mathrm{J}}/\sqrt{2}$ plotted[7] against β_* for four different values of κ_*. In Figure 11(a) and (b), with $\kappa_* \ll 1$, all five length scales are roughly equal, especially at smaller values of β_*. In Figure 11(d), with large bottom drag, the dependence of ℓ_0 on β_* deviates from that of the other length scales. This reflects the baroclinicity associated with strong bottom drag. There is good agreement between ℓ_{mix} and ℓ_{R} throughout parameter space except for small β_* and large κ_*. In this

---

[6] In the part of parameter space where LH03 might apply the flow is almost barotropic and roughly isotropic so $\mathcal{V} \approx \sqrt{2}V$.

[7] To estimate $\ell_{\mathrm{J}} \equiv L/n_{\mathrm{J}}$, the jet number n_{J} is determined by counting the number of jets in the equilibrated state. In the case where the system appears to be transitioning between a state with n and $n+1$ jets we follow Panetta and take $n_{\mathrm{J}} = n + 1/2$; no other fractional values are permitted.

regime the two scales deviate because β is too weak and friction is too strong for stable jets to form and thus ℓ_{R} has little meaning.

The results in Figure 11 pose a problem for LH03 since (30) implies that ℓ_{J} and ℓ_{R} should be significantly greater than the other three lengths, and this disparity should increase as κ_* is reduced. Figure 11 suggests a simpler result: all five lengths are equivalent when $\kappa_* \ll 1$. A comparison of ℓ_{mix} and ℓ_{R} for the 15 runs in the LH03 regime is shown in Figure 10(c).

4.2 Jet-scale eddies

We turn now to a more detailed analysis of the eddy length scales in a few particular runs. Embedded within the eastward flowing zonal jets are a series of large eddies, similar to atmospheric storms in a storm track (Figure 1(d) and (f)). These eddies are isotropic and have diameter of roughly $\pi\ell_J$. The strong eastward flow is observed to meander around these eddies.

In Figure 12 we show that the dominant contribution to the eddy heat flux comes from the jet-scale eddies. Beginning with 300 snapshots of $\psi'(x,y)$ and $\tau'(x,y)$, high-pass filtered fields, $\tilde{\psi}(x,y)$ and $\tilde{\tau}(x,y)$, are formed by setting the Fourier coefficients for all wavenumbers within a wavenumber circle of radius R to zero. The truncated heat flux $U^{-1}\left\langle \tilde{\psi}_x\tilde{\tau}\right\rangle \equiv \tilde{D}_\tau$ is calculated by integrating $\tilde{\psi}_x\tilde{\tau}$ over the domain and averaging over the 300 snapshots. By varying the radius R one can assess how different spatial scales contribute to the total heat flux.

The heat flux $U^{-1}\left\langle \tilde{\psi}_x \tilde{\tau} \right\rangle$ is plotted in Figure 12 as a function of R for three simulations. For wavenumbers less than[8] $k_{\mathrm{J}}\lambda$, indicated by the dotted lines, $\tilde{D}_\tau \approx D_\tau$, i.e. eddies larger than ℓ_{J} do not contribute to the heat flux. As R increases from k_J to $2k_J$, $\tilde{D}_\tau$ drops quickly to roughly 30% of D_τ. This demonstrates that jet-scale eddies, with a scale comparable to ℓ_{J}, are responsible for nearly 70% the heat flux in the equilibrated flow.

To summarize: the large-scale eddies evident in Figure 1(d), (f) and Figure 9(d) are responsible for a large fraction of the equilibrated meridional eddy heat flux. This confirms there is no separation between ℓ_{mix} and ℓ_{J}.

4.3 Eddy-zonal mean interactions

The jet-scale eddies also have a baroclinic component. Figure 13(a), a snapshot of the eddy baroclinic streamfunction $\tau' = \tau - \bar{\tau}$, indicates that baroclinic eddies show more anisotropy than those in the barotropic field (Figure 1(d). This anisotropy reflects eddy tilting by the zonal mean meridional shear and suggests that Reynold stress correlations are an important mechanism for forcing the zonal flow. Figure 13(b) shows a snapshot of the upper layer

---

[8] The jet wavenumber is $k_{\mathrm{J}} \equiv \ell_{\mathrm{J}}^{-1}$, where ℓ_{J} is defined in (25).

Reynolds stresses $u_1'v_1'$, which are also strongly tilted.

Since zonal jets spontaneously form in both the baroclinic and barotropic problem, it is tempting to think that the zonal mean dynamics of the baroclinic problem are dominated by the barotropic mode. To asses this hypothesis we analyze the the zonal energy balance, in layer form, by multiplying the upper and lower layer PV equations (46) and (47) by $\bar{\psi}_1$ and $\bar{\psi}_2$ respectively, and averaging over both space and time. This yields

$$\begin{aligned} \mathscr{Z}_t &= \left\langle \bar{u}_{1y}\left(\overline{u_1'v_1'}\right) + \bar{u}_{2y}\left(\overline{u_2'v_2'}\right) + \tfrac{1}{2}\left(\bar{u}_2 - \bar{u}_1\right)\left(\overline{\psi_1'\psi_{2x}'}\right)\right\rangle \\ &- \frac{\kappa}{2}\left\langle\left[\left(\sqrt{2}-1\right)\bar{\psi}_{1y} - \left(\sqrt{2}+1\right)\bar{\psi}_{2y}\right]^2\right\rangle , \end{aligned} \tag{35}$$

where $\mathscr{Z}$ is the zonal energy

$$\mathscr{Z} \equiv \tfrac{1}{2}\left\langle \bar{\psi}_{1y}^2 + \bar{\psi}_{2y}^2 + \tfrac{1}{2}\lambda^{-2}\left(\bar{\psi}_1 - \bar{\psi}_2\right)^2\right\rangle . \tag{36}$$

The first three terms on the RHS of (35) are exchanges of energy between zonal and eddy components. The first two are sources of zonal energy due to non-zero Reynolds stress correlations caused by eddy tilting on the jet flanks. This process results in an up-gradient flux of momentum that has been described as negative viscosity (McIntyre 1970; Manfroi & Young 1999; Dritschel *et al.* 2006) responsible for the remarkable persistence and stability of zonal jets. The third term is a sink of zonal-mean energy representing extraction of potential energy stored in the mean temperature gradient through baroclinic instability. The final terms are dissipation of $\mathcal{Z}$ by bottom friction.

Figure 13(a) shows the upper and lower layer energy transfer terms for two simulations, one with many steady jets, $\beta_* = 0.75$ and $\kappa_* = 0.08$, and a second that conforms to the LH03 regime, $\beta_* = 0.25$ and $\kappa_* = 0.04$. Figure 13 illustrates the motivation for writing (35) in terms of layers rather than modes: nearly all energy transfer from the eddies into the zonal-mean flow occurs in the upper layer. This is true even when the zonal flow is almost completely barotropic as in panel (b) (cf. Figure 9(a)). Figure 13 confirms that the regions where upper layer energy transfer is largest are located on both flanks of the eastward jets where the meridional shear is strongest. Figure 13 shows that the energy transfer into the zonal-mean flow occurs mainly in the upper layer, even though the zonal flow is dominantly barotropic. Thus the equilibrated system depends crucially on the underlying baroclinicity of the jet-scale eddies.

5 Domain size, resolution and hyperviscosity

To this point we have suppressed reference to the non-dimensional parameter L/λ. However, a diffusive parameterization is well-founded only if D_τ is independent of domain size and of the hyperviscosity and resolution (Haidvogel & Held 1980). Thus before one trusts the data in Figure 3 one must show that large changes in the domain size L make only small changes in D_τ.

Some results of this sensitivity study are summarized in Figure 14 which shows the barotropic jet velocity $u_J(y) \equiv -\bar{\psi}_y$ and D_τ for six simulations at $\beta_* = 0.5$ and $\kappa_* = 0.02$. In each case the time averaging was completed for at least $1000\lambda/U$. The length of the u_J-profile indicates the size of the domain, which varies between $2\pi \times (12.5\lambda)$ and $2\pi \times (50\lambda)$. The curves have been translated so that the dotted lines mark the zero crossings of $u_J(y)$. Run XI, which is the simulation in Figure 3, has five stable jets. The other five u_J-profiles show some indication of vacillation in n_J. Since run XI is stable with five jets, it is perhaps not surprising that runs XII and XIII, which halve the domain size, have between two and three jets. Still, the magnitude of the zonal flow is similar in each simulation and the indicated values of $D_{\tau *}$ in Figure 14 are within 10% of the $D_\tau^{XI} = 2.217U\lambda$. Motivated by these results we have adopted the policy of trusting a data point in Figure 3 if the variation in D_τ resulting from halving and doubling the domain size is $\pm 10\%$. Thus according to this criterion run XI is trustworthy.

Runs with the smallest values of bottom friction in Figure 3, namely $\kappa_* = 0.02$ and 0.04, fail the $\pm 10\%$ criterion if β is also sufficiently small. Thus in Figure 3 we have not extended our survey of D_τ to $\beta_* < 0.25$ *and*

$\kappa_* \leq 0.04$. Indeed with $\kappa \leq 0.04$ and $\beta = 0$ we are firmly in the global mixing regime described by Thompson & Young (2006). In this regime there are only a few vortices in the domain and statistical descriptions based on an eddy diffusivity are meaningless because there is no scale separation between L and the mixing length. The data points in Figure 3(a) that extend to values of $\beta_* < 0.25$ all have largish values of κ_* so that these simulations are within Thompson & Young's local mixing regime even at $\beta_* = 0$.

To further probe sensitivity to domain size, resolution and hyperviscosity, we conducted the suite of 24 simulations summarized in Table 1; the main simulations appearing in Figure 3 are shown Table 1 in boldface type. In 22 of these simulations we take $\kappa_* = 0.02$ and we obtain at least five runs at each of $\beta_* = 0.25$, 0.5, 0.75 and 1. This study tests different combinations of domain size L, numerical resolution, and hyperviscosity ν. For example, at $\beta_* = 0.5$, runs VIII, XI and XIII have the same resolution, whereas runs IX, X and XII have double resolution.

Table 1 lists domain-averaged statistics for a number of key quantities. With the exception of the run at $\beta_* = 0.25$ and $\kappa_* = 0.02$, domain-averaged statistics are constant to within roughly ±10% and for simulations with $\beta_* \geq 0.5$, all quantities are constant to within ±5%. Deviation between the different simulations are most likely related to differences in the hyperviscous contribution to the dissipation which is listed in the final column of Table 1. Naturally the higher resolution runs have a smaller ratio of hyper-viscous dissipation to total dissipation (although the coefficient ν is adjusted for domain size). It is satisfying that if the domain size is fixed and ν is varied by an order of magnitude, eddy statistics change only a little.

The exceptional run in Table 1 is at $\beta_* = 0.25$ and $\kappa_* = 0.02$. In this case doubling L increases D_τ by 20%. This is the most sensitive data point in Figure 3(a)[9] and accordingly we have flagged this data point Figure 3(b) with a question mark. To confirm that a well defined eddy diffusivity exists at $\beta_* = 0.25$, we tested the data point with $\kappa_* = 0.04$ by doubling the domain size (see the two italic rows in table 1). This results in a 5% increase in D_τ and supports the view that the run at $\beta_* = 0.25$ and $\kappa_* = 0.04$ is trustworthy.

To summarize, based on the results in Table 1 we conclude that the eddy diffusivity D_τ is independent of domain size to within ±10% for simulations with $\beta_* > 0.25$ or $\kappa_* > 0.02$.

---

[9] The fact that $D_\tau/U\lambda$ is larger in the large-domain simulation (run I in Table 1) suggests that the leveling off of the slope at $\kappa_* = 0.02$ in the $\beta_* = 0.25$ series of Figure 3(b) is the first indication of domain dependence.

6 Conclusions

In this computational study we have shown that D_τ depends on both β_* and κ_* over a broad region of parameter space. D_τ has a greater sensitivity to changes in β_* than to changes in κ_*. While increases in β_* result in a monotonic decrease in the eddy heat flux, the bottom friction dependence is more complicated with D_τ increasing (decreasing) in response to increasing κ_* at β_* greater than (less than) β_*^{piv}. Our simulations indicate a regime in which D_τ depends weakly on bottom drag and this is consistent with the arguments underlying the LH03 parameterization. However the behavior of other statistics, such as the mixing length and the eddy velocity, shows an uncomfortable dependence on κ_*, which is not consistent with LH03.

In one respect the numerical simulations are simpler than the LH03 theory: at small κ_* all of the length scales in the problem converge to a common value. For example the mixing length ℓ_{mix} is equivalent to the jet scale ℓ_{J}. This simplicity is off-set by the complicated dependence of the correlation c_τ on κ_* and β_*. The variation in c_τ cancels significant variations in V and ℓ_{mix} so that $D_\tau = c_\tau \ell_{\mathrm{mix}} V$ has a smaller sensitivity to κ_*. The upshot is that a successful theory of eddy heat fluxes cannot treat c_τ as a dimensionless constant of order unity. We believe that this correlation is a signature of the jet-scale baroclinic waves which are largely responsible for the net heat flux.

Perhaps the most novel result presented here is the importance of the baroclinic mode in determining the eddy heat flux and other important descriptors of the equilibrated flow. In simulations in which β leads to the spontaneous generation of zonal jets, it is inappropriate to view the baroclinic mode as simply an innocuous deformation-scale mechanism for energizing the inverse cascade of the barotropic mode. This view fails in at least two important respects:

(a) total dissipation ε cannot be easily related to the barotropic dissipation ε_ψ except in a corner of the parameter space;

(b) the zonal mean flow is energized by upper-layer Reynolds stresses (rather than barotropic Reynolds stresses).

Regarding point (b), previous theories (Vallis & Maltrud 1993; Lapeyre & Held 2003) assume that all energy in the zonal modes results from transfers out of the *barotropic* eddies at a wavenumber k_β determined by the strength of β. However, results from our simulations summarized in Figure 13 show that *upper layer* Reynolds stress correlations are responsible for almost all of the energy transfer into the zonal mean component. If one expresses this upper-layer transfer in terms of modes then it projects in a complicated fashion on both the barotropic and baroclinic modes. Thus it is misleading to view the excitation of zonal mean flows as a purely barotropic process.

The importance of the baroclinic mode is in some ways not too surprising since differences in PV transport between upper and lower layers have been reported prior to this study (Lee & Held 1993, Greenslade & Haynes 2006). In fact, it is exactly this behavior led LH03 to apply a turbulent diffusivity to the *lower* layer flow, which is more turbulent and less wave-like, in an attempt to avoid complications arising from the spontaneous formation of zonal jets.

However, throughout parameter space surveyed here, new models of baroclinic turbulence are required to address the added complications of energy dissipation and energy transfer by the baroclinic mode. Any complete model of β-plane baroclinic turbulence must also account for the formation of zonal jets and the strong meridional potential vorticity and velocity gradients associated with them. The recent work of Zurita-Gotor (2006), in which the potential vorticity curvature induced by jet formation is included in scalings of the eddy heat flux, is a step in this direction.

Acknowledgements

We thank Lien Hua and Patrice Klein for providing the spectral code used in this work. We have benefitted from conversations with Paola Cessi, Rick

Salmon, Isaac Held, Guillaume Lapeyre, Geoff Vallis, Shaffer Smith and Boris Galperin

This work was supported by National Science Foundation grants OCE-0220362 and OCE-0100868. AFT also gratefully acknowledges the support of an NDSEG Fellowship.

A The two-mode equations of motion

The derivation of the modal equations used in our study is based on Flierl (1978), and also includes forcing terms that arise when there is a mean shear in the basic state as discussed in Hua & Haidvogel (1986). Our equations differ from Hua & Haidvogel only in the form of the hyperviscous term, which is used to absorb enstrophy cascading to the highest wavenumbers. The main difference between the modal decomposition used here and the method used by Larichev and Held (1995) appears in the coefficients of the bottom drag term as shown below.

The continuous quasigeostrophic equations are written as

$$\frac{\partial}{\partial t}Q + J(\Psi, Q) = -\nu \nabla^8 Q \,. \tag{37}$$

Here J represents the Jacobian, $J(a,b) \equiv a_x b_y - a_y b_x$, Ψ is the stream function such that $u = -\Psi_y$ and $v = \Psi_x$, and

$$Q = \nabla^2 \Psi + (f/N)^2 \, \Psi_{zz} \,, \tag{38}$$

is the potential vorticity. We consider dynamics on a β-plane, and take the Brunt-Vaisala frequency N to be constant. The coefficient of hyperviscosity is given by ν and H is the depth of the ocean. The Rossby deformation radius is $\lambda = NH/\pi$.

Using a truncated modal expansion in the vertical, we consider the barotropic and first baroclinic modes with a mean shear. We write this as

$$\Psi(x, y, z, t) = \psi(x, y, t) + [-Uy + \tau(x, y, t)]\,\sqrt{2}\cos\left(\frac{\pi z}{H}\right)\,, \tag{39}$$

where ψ and τ are the perturbation stream functions of the barotropic and baroclinic modes respectively. The factor of $\sqrt{2}$ arises from normalization of the modes (Flierl 1978). The corresponding potential vorticity is

$$Q = \nabla^2\psi + \left(\nabla^2\tau - \lambda^{-2}\tau + U\lambda^{-2}y\right)\sqrt{2}\cos\left(\frac{\pi z}{H}\right)\,. \tag{40}$$

We now apply the modal decomposition of Ψ to the the quasigeostrophic equation and project in the barotropic and baroclinic modes. The frictional, or Ekman drag, terms arise from the bottom boundary condition,

$$w(x, y, -H, t) = \delta_E \nabla^2\Psi(x, y, -H, t)\,, \tag{41}$$

where δ_E is the Ekman layer depth. In our model the Ekman drag coefficient is defined by $\kappa = f\delta_E/H$.

The resulting modal equations are:

$$\nabla^2\psi_t + J(\psi, \nabla^2\psi) + J(\tau, \nabla^2\tau) + U\nabla^2\tau_x + \beta\psi_x = -\kappa\nabla^2(\psi - \varkappa\tau) - \nu\nabla^8(\nabla^2\psi)\,, \tag{42}$$

and

$$\begin{aligned}\left(\nabla^2-\lambda^{-2}\right)\tau_t &+ J(\psi,(\nabla^2-\lambda^{-2})\tau)+J(\tau,\nabla^2\psi)+U\left(\nabla^2+\lambda^{-2}\right)\psi_x+\beta\tau_x\\ &= \varkappa\kappa\nabla^2(\psi-\varkappa\tau)-\nu\nabla^8(\nabla^2-\lambda^{-2})\tau\,. \qquad (43)\end{aligned}$$

The variable $\varkappa$ above controls the projection of the bottom drag onto the layers. The modal projection in (39) and (40) results in $\varkappa=\sqrt{2}$. To limit the effect of bottom drag to the lower layer, set $\varkappa=1$ (as in Larichev & Held 1995).

To make a comparison with LH03 we introduce equivalent layer variables

$$\psi_1=\psi+\tau\,, \qquad \psi_2=\psi-\tau\,, \qquad (44)$$

and the corresponding potential vorticities

$$\begin{aligned} q_1 &= \nabla^2\psi_1+\tfrac{1}{2}\lambda^{-2}(\psi_2-\psi_1)=\nabla^2\psi+(\nabla^2\tau-\lambda^{-2}\tau)\,,\\ q_2 &= \nabla^2\psi_2+\tfrac{1}{2}\lambda^{-2}(\psi_1-\psi_2)=\nabla^2\psi-(\nabla^2\tau-\lambda^{-2}\tau)\,. \qquad (45)\end{aligned}$$

The layer equations are obtained by adding and subtracting (42) and (43):

$$q_{1t}+Uq_{1x}+G_1\psi_{1x}+J(\psi_1,q_1) = Diss_1\,, \qquad (46)$$

$$q_{2t}-Uq_{2x}+G_2\psi_{2x}+J(\psi_2,q_2) = Diss_2\,. \qquad (47)$$

Above, the PV gradients are

$$G_1=\beta+\lambda^{-2}U\,, \qquad G_2=\beta-\lambda^{-2}U\,, \qquad (48)$$

and the dissipative terms are

$$\begin{aligned} Diss_1 &\equiv (\varkappa - 1)\kappa\nabla^2\psi_\varkappa - \nu\nabla^8 q_1\,, && (49)\\ Diss_2 &\equiv -(\varkappa + 1)\kappa\nabla^2\psi_\varkappa - \nu\nabla^8 q_2\,, && (50) \end{aligned}$$

with

$$\psi_\varkappa \equiv \psi - \varkappa\tau = \frac{\varkappa+1}{2}\psi_2 - \frac{\varkappa-1}{2}\psi_1\,. \tag{51}$$

Notice that the velocity jump between the two layers is $2U$.

The energy balance is obtained in the standard manner by multiplying the barotropic and baroclinic modal equations by ψ and τ respectively and averaging over space. In a statistically steady state the energy balance requires

$$U\lambda^{-2}\left\langle \psi_x\tau\right\rangle = \kappa\left\langle |\nabla\psi_\varkappa|^2\right\rangle + hyp\nu\,, \tag{52}$$

where $\psi_\varkappa \equiv \psi - \varkappa\tau$. The hyperviscous term in (52) is

$$hyp\nu = \nu\left\langle |\nabla\nabla^4\psi|^2\right\rangle + \nu\left\langle |\nabla\nabla^4\tau|^2\right\rangle + \nu\lambda^{-2}\left\langle \left(\nabla^4\tau\right)^2\right\rangle\,. \tag{53}$$

Setting $\varkappa = \sqrt{2}$ we obtain (2).

We record some well known identities which are easily obtained using the layer variables. First and foremost, the three different fluxes are all related by:

$$\lambda^{-2}\langle\psi_x\tau\rangle = \tfrac{1}{2}\lambda^{-2}\langle\psi_{2x}\psi_1\rangle = \langle v_2 q_2\rangle = -\langle v_1 q_1\rangle\,. \tag{54}$$

The corresponding eddy diffusivities are defined by

$$\langle v_1 q_1 \rangle = -D_1 G_1 \quad (\text{definition of } D_1)\,, \tag{55}$$

$$\langle v_2 q_2 \rangle = -D_2 G_2 \quad (\text{definition of } D_2)\,, \tag{56}$$

$$\langle \psi_x \tau \rangle = -D_\tau U \quad (\text{definition of } D_\tau)\,. \tag{57}$$

Using (54), the three diffusivities are related by

$$D_\tau = (1+\beta_*)D_1 = (1-\beta_*)D_2\,, \tag{58}$$

where $\beta_* \equiv \beta\lambda^2/U$. There are some problems with these diffusivities e.g., when $\beta_* = 1$ the instability is still active and so the three fluxes are nonzero and related by (54). This forces the conclusion that $D_2 = \infty$, not $D_2 = 0$. For this reason we prefer to deal exclusively with D_τ.

References

[1] Arbic, B. K. & Flierl, G. R., 2004: Effects of mean flow direction on energy, isotropy, and coherence of baroclinically unstable beta-plane geostrophic turbulence, *J. Phys. Oceanogr.*, **34**, 77-93.

[2] Dritschel, D. G., Haynes, P. H. & McIntyre, M. E., 2006: Multiple jets as PV staircases: the Phillips effect and the resilience of eddy-transport barriers, Submitted to the Savannah Special Issue of *J. Atmos. Sci.*

[3] Flierl, G. R., 1978: Models of vertical structure and the calibration of two-layer models. *Dyn. Atmos. Oceans*, **2**, 342-381.

[4] Greenslade, M. D. & Haynes, P. H., 2006: Vertical transition in transport and mixing in baroclinic flows, Submitted to the Savannah Special Issue of *J. Atmos. Sci.*

[5] Haidvogel D. B. & Held, I. M., 1980: Homogeneous quasi-geostrophic turbulence driven by a uniform temperature gradient, *J. Atmos. Sci.*, **37**, 2644-2660.

[6] Held, I. M. & Larichev, V. D., 1996: A scaling theory for horizontally homogeneous, baroclinically unstable flow on a beta plane, *J. Atmos. Sci.*, **53**, 946-952.

[7] Holopainen, E. O., 1961: On the effect of friction in baroclinic waves, *Tellus*, **13**, 363-367.

[8] Hua, B. L. & Haidvogel, D. B., 1986: Numerical simulations of the vertical structure of quasi-geostrophic turbulence, *J. Atmos. Sci.*, **43**, 2923-2936.

[9] Lapeyre, G. & Held, I. M., 2003 (herein LH03): Diffusivity, kinetic energy dissipation, and closure theories for the poleward eddy heat flux, *J. Atmos. Sci.*, **60**, 2907-2916.

[10] Larichev, V. & Held, I.M., 1995: Eddy amplitudes and fluxes in a homogeneous model of fully developed baroclinic instability, *J. Phys. Oceanogr.*, **25**, 2285-2297.

[11] Lee, S., 1997: Maintenance of multiple jets in a baroclinic flow, *J. Atmos. Sci.*, **54**, 1726-1738.

[12] Lee, S., & Held, I. M., 1993: Baroclinic wave packets in models and observations, *J. Atmos. Sci.*, **50**, 1413-1428.

[13] MANFROI, A. J. & YOUNG, W. R., 1999: Slow evolution of zonal jets on the beta plane, *J. Atmos. Sci.*, **56**, 784-800.

[14] MCINTYRE, M. E., 1970: On the non-separable baroclinic parallel flow instability problem, *J. Fluid Mech.*, **40**, 273-306.

[15] PANETTA, L., 1993: Zonal jets in wide baroclinically unstable regions: persistence and scale selection, *J. Atmos. Sci.*, **50**, 2073-2106.

[16] PAVAN, V. & HELD, I. M., 1996: The diffusive approximation for eddy fluxes in baroclinically unstable jets, *J. Atmos. Sci.*, **53**, 1262-1272.

[17] PEDLOSKY, J., 1987: *Geophysical Fluid Dynamics*, 2nd ed. Springer-Verlag, 710pp.

[18] RHINES, P. B., 1975: Waves and turbulence on a beta-plane, *J. Fluid Mech.* **69**, 417-443.

[19] RHINES, P. B., 1977: The dynamics of unsteady currents, *The Sea*, Vol. 6, E. A. Goldberg, I. N. McCane, J. J. O'Brien & J. H. Steele, Eds., Wiley, 189-318.

[20] SALMON, R., 1980: Baroclinic instability and geostrophic turbulence, *Geophys. Astrophys. Fluid Dyn.*, **15**, 167-211.

[21] Smith, K. S., Boccaletti, G., Henning, C. C., Marinov, I., Tam, C. Y., Held, I. M. & Vallis, G.K., 2002: Turbulent diffusion in the geostrophic inverse cascade, *J. Fluid Mech.,* **469**, 13-48.

[22] Thompson, A. F., 2006: Eddy fluxes in baroclinic turbulence. Ph. D. dissertation, University of California, San Diego. 182 pp.

[23] Thompson, A. F. & Young, W. R., 2006: Scaling baroclinic eddy fluxes: vortices and energy balance, *J. Phys. Oceanogr.*, **36**, 720-738.

[24] Vallis, G. K. & Maltrud, M. E., 1993: Generation of mean flow and jets on a beta plane and over topography, *J. Phys. Oceanogr.*, **23**, 1346-1362.

[25] Williams, G. P., 1979: Planetary circulations: 2, The Jovian quasi-geostrophic regime, *J. Atmos. Sci.*, **36**, 932-968.

[26] Zurita-Gotor, P., 2006: The relation between baroclinic adjustment and turbulent diffusion in the two layer model, *J. Atmos. Sci.*, In press.

Figure captions

Table 1. Eddy statistics for sensitivity study simulations. All runs have $\kappa\lambda/U = 0.02$ except for two runs in italics which have $\kappa\lambda/U = 0.04$. The bold entries indicate the main simulations shown in Figure 3.

Fig. 1. (*a*) Growth rates of the linear baroclinic instability for three values of $\beta_* \equiv \beta\lambda/U$ all with $\kappa_* \equiv \kappa\lambda/U = 0.02$; bottom friction produces instability at the frictionless critical value $\beta_* = 1$. (*b*) Three time series of the eddy diffusivity $D_\tau/U\lambda$ all at $\kappa_* = 0.02$. The "instantaneous" diffusivity is defined by taking $\langle\rangle$ in (1) only as an (x, y) average. (*c*) Hovmoller diagram of the zonally averaged barotropic velocity $-\bar{\psi}_y$ with $\beta_* = 0.5$, $\kappa_* = 0.02$. (*d*) Snapshot of the eddy streamfunction $\psi' = \psi - \bar{\psi}$ for the simulation in panel (*c*); ψ' is dominated by isotropic eddies with the same scale as the zonal jets in panel (*c*). Panels (*e*) and (*f*) are the same as (*c*) and (*d*) but for a simulation with $\beta_* = 1$ and $\kappa_* = 0.02$.

Fig. 2. Zonal mean fields at the parameter values indicated in panels (*c*) and (*f*). Panels (*a*) and (*d*) show the velocities, $\mathcal{U}_n = U_n - \bar{\psi}_{ny}$ in the upper (solid) and lower (dashed) layers. The basic-state velocity jump between the layers, $2U$, is indicated by the dotted lines. Panels (*b*) and (*e*) show the PV gradients in the upper and lower layers. The basic state gradients,

$1 + \beta_*$ and $1 - \beta_*$, are indicated by dotted lines. In panels (c) and (f) the thick solid curve is the barotropic PV, $\beta y + \bar{\psi}_{yy}$; the thin jagged curve is an instantaneous section of barotropic PV, $\beta y + \nabla^2\psi$, along the line $x = 0$.

Fig. 3. (a) Survey of the non-dimensional meridional eddy heat flux $D_\tau/U\lambda$ at 110 different values of the parameters β_* and κ_*. The dashed curve indicates the D_τ parameterization in (11) (with $c = 1.65$). The dotted line is an empirical fit $0.12\beta_*^{-4}$. At $\beta_{\mathrm{pivot}} = 0.72$, there is weak dependence on κ_*. Data at five values of β_* (indicated by the dotted lines) are expanded in panel (b) to illustrate the weaker but still significant dependence on κ_*. The point at $\beta_* = 0.25$ and $\kappa_* = 0.02$ is flagged with a "?" to indicate possible dependence on domain size (see section **5**).

Fig. 4. The ratio of the LHS of (8) to the RHS.

Fig. 5. (a) Ratio of terms in the energy balance approximation $U^2 D_\tau/\lambda^2 \approx \varepsilon$. The systematic departure from 1 is because the hyperviscous dissipation is not included in definition of ε in (3). (b) The ratio $D_2 \propto \varepsilon^{3/5}\beta^{-4/5}$.

Fig. 6. Ratio of the dissipation by the barotropic mode ε_ψ defined in (12) to the total dissipation ε defined in (3).

Fig. 7. Negative correlation $-\langle\zeta\tau\rangle/\sqrt{\langle\zeta^2\rangle\langle\tau^2\rangle}$ between the barotropic

vorticity ζ and the temperature τ for both zonally-averaged (solid symbols) and eddy (open symbols) components of the flow.

Fig. 8. Open symbols show $\varepsilon_\psi/\varepsilon$ for the 15 runs which come close to satisfying $\varepsilon_\psi/\varepsilon \approx 1$. The closed symbols show $\varepsilon_{\rm J}/\varepsilon$ where $\varepsilon_{\rm J} \equiv \kappa u_{\rm J}^2$ is the dissipation in the zonal mean flow.

Fig. 9. The run with $\kappa_* = 0.04$ and $\beta = 0.25$. (*a*) Upper (solid) and lower (dashed) zonal mean velocities; the zonal mean flow is almost barotropic and much faster than the basic state velocity jump $2U$ which is indicated by the dotted lines. (*b*) The zonal mean PV gradients upper (solid) and lower (dashed) layers. (*c*) A Hovmoller plot showing the meandering of the zonal jets. (*d*) A snapshot of the barotropic eddy streamfunction ψ'.

Fig. 10. (*a*) An expanded view of the eddy diffusivity for the 15 runs defined by (18). The dashed curve is the LH03 parameterization (11) and the dotted curve is the empirical fit $0.12\beta_*^{-4}$. The open symbols in panels (*b*), (*c*) and (*d*) show the statistics defined in (19) through (21). The filled symbols in panel (*c*) show the Rhines scale $\ell_{\rm R}$ as defined in (33).

Fig. 11. Eddy length scales $\ell_{\rm mix}$ (20), $2\ell_{\rm LH}$ (31), ℓ_0 (32), $\ell_{\rm R}$ (33) and $\ell_{\rm J}/\sqrt{2}$ (25) as a function of $\beta\lambda^2/U$ at four different values of $\kappa\lambda/U$. We use

$2\ell_{\mathrm{LH}}$ to give good agreement with the other length scales. In panels (a) and (b) the five lengths converge to a common value as κ_* and β_* decrease.

Fig. 12. (a) The truncated eddy heat flux $\tilde{D}_\tau/U\lambda$ as a function of the radius of the excluded wavenumber circle R for three simulations. Truncated fields $\tilde{\psi}$ and $\tilde{\tau}$ are formed by setting Fourier coefficients for wavenumbers less than R equal to zero. The time and spatial average $\left\langle \tilde{\psi}_x\tilde{\tau} \right\rangle$ is $U^2\lambda^{-2}\tilde{D}_\tau$; for the $\circ$'s, $\tilde{D}_\tau$ is divided by a factor of 6. The jet wavenumber $k_J\lambda$ for each simulation is given by the dotted lines. (b) The same data as in panel (a) shown on log-log axes.

Fig. 13. (a) Snapshot of the eddy temperature field (baroclinic streamfunction) $\tau' = \tau - \bar{\tau}$ for the simulation $\beta_* = 0.5$ and $\kappa_* = 0.02$. The baroclinic field is less isotropic than its barotropic counterpart in Figure 1(d). (b) Snapshot of the upper layer Reynolds stresses $u_1'v_1'$ for the same simulation. (c) Zonal and time averages of the energy transfer terms in upper (solid line) and lower (dashed line) layers for the simulation $\beta_* = 0.75$ and $\kappa_* = 0.08$. The barotropic zonal velocity divided by a factor of 2 is given by the dotted line. (d) Same as panel (c) for the simulation $\beta_* = 0.25$ and $\kappa_* = 0.02$. These curves are noisier because the jets are less steady (Figure 9). Note *upper layer* eddy shearing on the jet flanks plays an important role in energizing

the zonal mean flow.

Fig. 14. Zonal and time-averaged barotropic velocities $u_J(y) \equiv -\bar{\psi}_y$ for sensitivity studies (VIII-XIII) listed in Table 1 with $\beta_* = 0.5$. For clarity the curves have been translated horizontally; intersections with the dotted lines indicate zero crossings u_J. The five runs correspond to varying domain sizes and resolutions. Most runs suffer from quantization problems that may be related to differences in the hyperviscosity parameter. Run XI is stable and has an odd number of jets, therefore a quantization problem may be expected when halving the domain size (Runs XII and XIII). The domain-averaged heat flux is indicated for each simulation; domain-averaged statistics are within ±5% for all runs with $\beta_* > 0.25$ (see Table 1).

Table 1: Eddy statistics for sensitivity study simulations. All runs have $\kappa\lambda/U = 0.02$ except for two runs in italics which have $\kappa\lambda/U = 0.04$. The bold entries indicate the main simulations shown in Figure 3.

	$\beta\lambda^2/U$	L/λ	ν/UL^7	Grid points	$D_\tau/U\lambda$	V/U	u_J/U	$\varepsilon_\nu/\varepsilon_{\text{tot.}}$
I	1/4	50	10^{-17}	512^2	39.48	19.42	35.38	0.0493
II	1/4	25	10^{-15}	512^2	36.50	20.53	33.13	0.0443
III	**1/4**	**25**	**10^{-15}**	**256^2**	**34.43**	**18.89**	**33.20**	**0.0575**
IV	1/4	12.5	10^{-13}	256^2	34.72	20.75	34.28	0.0285
V	1/4	12.5	10^{-13}	128^2	31.39	18.26	31.32	0.109
VI	*1/4*	*50*	*10^{-17}*	*512^2*	*35.68*	*17.35*	*18.65*	*0.0538*
VII	*1/4*	*25*	*10^{-15}*	*256^2*	*34.00*	*16.04*	*20.72*	*0.0557*
VIII	1/2	50	10^{-17}	512^2	2.056	5.092	8.848	0.0562
IX	1/2	25	10^{-17}	512^2	2.276	5.478	9.398	0.0148
X	1/2	25	10^{-15}	512^2	2.085	5.170	8.911	0.0395
XI	**1/2**	**25**	**10^{-15}**	**256^2**	**2.217**	**5.534**	**9.182**	**0.0562**
XII	1/2	12.5	10^{-13}	256^2	1.933	5.143	8.540	0.0380
XIII	1/2	12.5	10^{-13}	128^2	1.990	5.176	8.635	0.0563
XIV	3/4	50	10^{-17}	512^2	0.268	2.567	3.536	0.0575
XV	3/4	25	10^{-15}	512^2	0.269	2.608	3.539	0.0480
XVI	3/4	25	10^{-14}	256^2	0.251	2.577	3.422	0.0927
XVII	**3/4**	**25**	**10^{-15}**	**256^2**	**0.277**	**2.590**	**3.591**	**0.0601**
XVIII	3/4	12.5	10^{-13}	256^2	0.287	2.825	3.593	0.0456
XIX	3/4	12.5	10^{-13}	128^2	0.274	2.610	3.600	0.0588
XX	1	50	10^{-17}	512^2	0.0659	1.756	2.202	0.0772
XXI	1	25	10^{-15}	512^2	0.0640	1.713	2.178	0.0581
XXII	**1**	**25**	**10^{-15}**	**256^2**	**0.0620**	**1.681**	**2.132**	**0.0821**
XXIII	1	12.5	10^{-13}	256^2	0.0671	1.884	2.192	0.0673
XXIV	1	12.5	10^{-13}	128^2	0.0622	1.668	2.167	0.1121

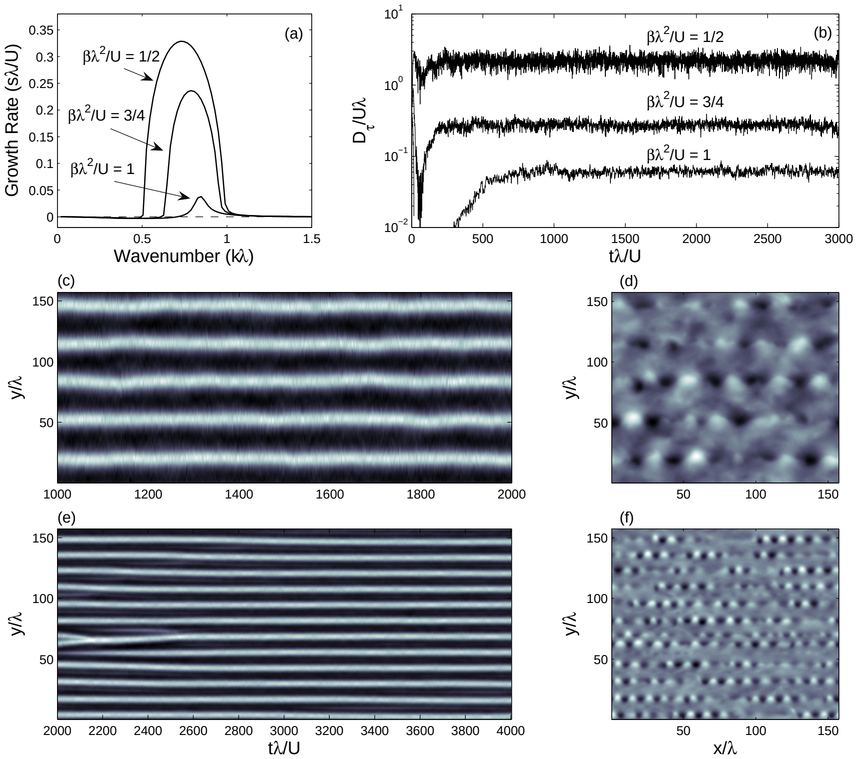

Figure 1: (a) Growth rates of the linear baroclinic instability for three values of $\beta_* \equiv \beta\lambda/U$ all with $\kappa_* \equiv \kappa\lambda/U = 0.02$; bottom friction produces instability at the frictionless critical value $\beta_* = 1$. (b) Three time series of the eddy diffusivity $D_\tau/U\lambda$ all at $\kappa_* = 0.02$. The "instantaneous" diffusivity is defined by taking $\langle\rangle$ in (1) only as an (x, y) average. (c) Hovmoller diagram of the zonally averaged barotropic velocity $-\bar{\psi}_y$ with $\beta_* = 0.5$, $\kappa_* = 0.02$. (d) Snapshot of the eddy streamfunction $\psi' = \psi - \bar{\psi}$ for the simulation in panel (c); ψ' is dominated by isotropic eddies with the same scale as the zonal jets in panel (c). Panels (e) and (f) are the same as (c) and (d) but for a simulation with $\beta_* = 1$ and $\kappa_* = 0.02$.

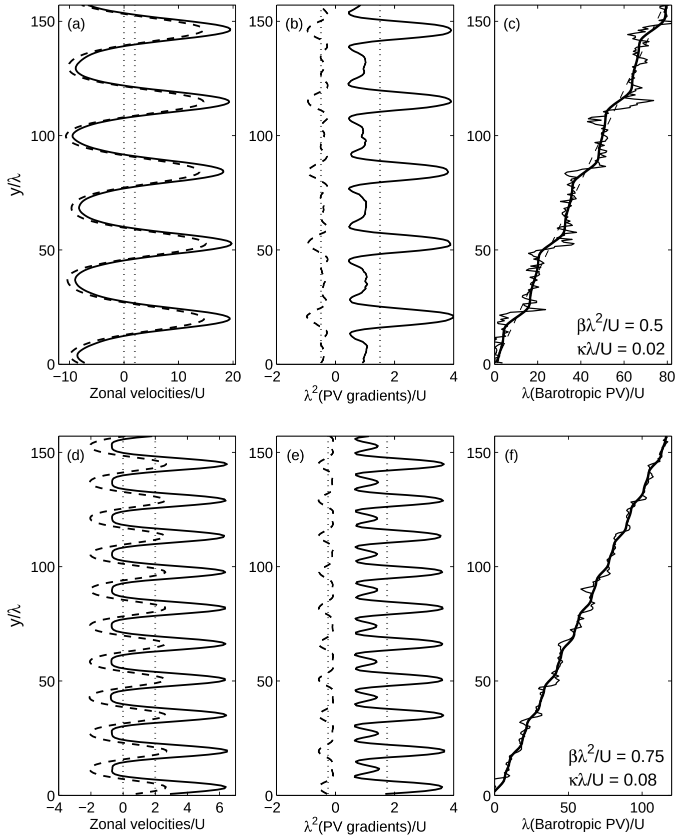

Figure 2: Zonal mean fields at the parameter values indicated in panels (c) and (f). Panels (a) and (d) show the velocities, $\mathcal{U}_n = U_n - \bar{\psi}_{ny}$ in the upper (solid) and lower (dashed) layers. The basic-state velocity jump between the layers, $2U$, is indicated by the dotted lines. Panels (b) and (e) show the PV gradients in the upper and lower layers. The basic state gradients, $1 + \beta_*$ and $1 - \beta_*$, are indicated by dotted lines. In panels (c) and (f) the thick solid curve is the barotropic PV, $\beta y + \bar{\psi}_{yy}$; the thin jagged curve is an instantaneous section of barotropic PV, $\beta y + \nabla^2\psi$, along the line $x = 0$.

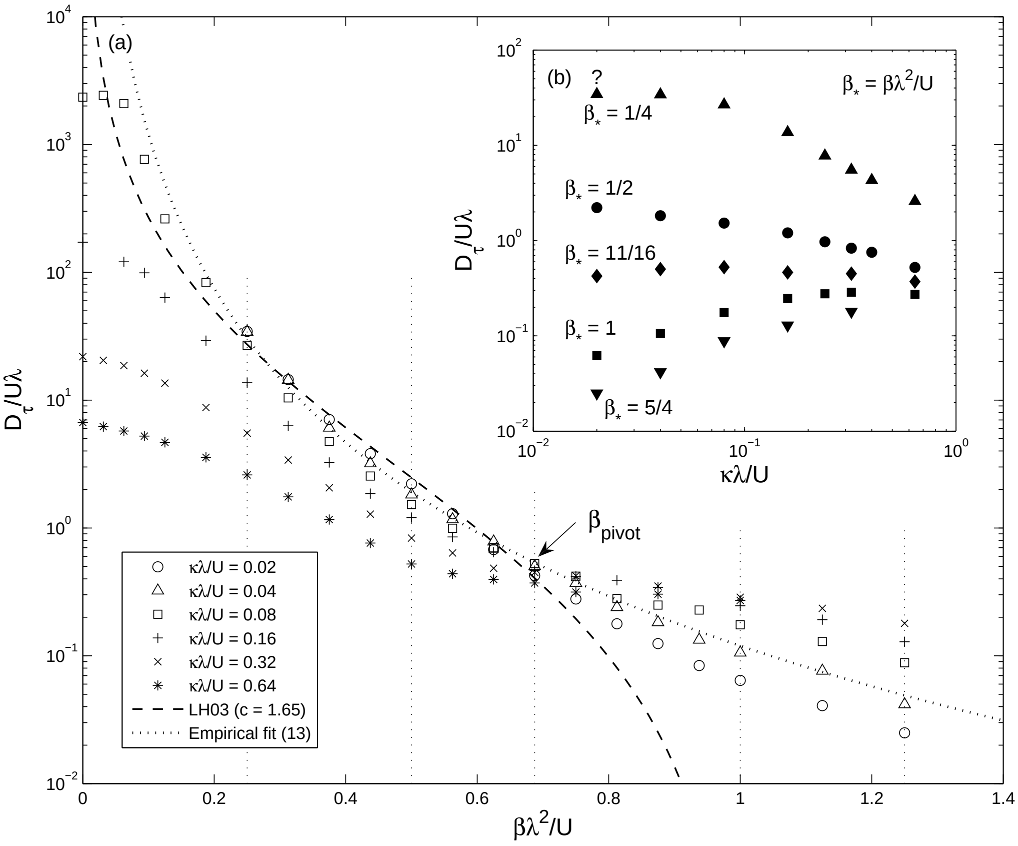

Figure 3: (*a*) Survey of the non-dimensional meridional eddy heat flux $D_\tau/U\lambda$ at 110 different values of the parameters β_* and κ_*. The dashed curve indicates the D_τ parameterization in (11) (with $c = 1.65$). The dotted line is an empirical fit $0.12\beta_*^{-4}$. At $\beta_{\rm pivot} = 0.72$, there is weak dependence on κ_*. Data at five values of β_* (indicated by the dotted lines) are expanded in panel (*b*) to illustrate the weaker but still significant dependence on κ_*. The point at $\beta_* = 0.25$ and $\kappa_* = 0.02$ is flagged with a "?" to indicate possible dependence on domain size (see section **5**).

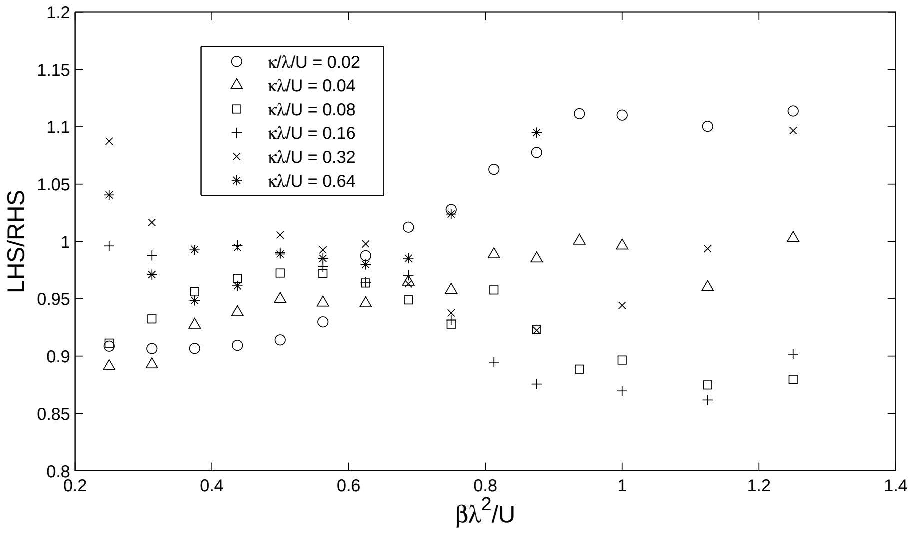

Figure 4: The ratio of the LHS of (8) to the RHS.

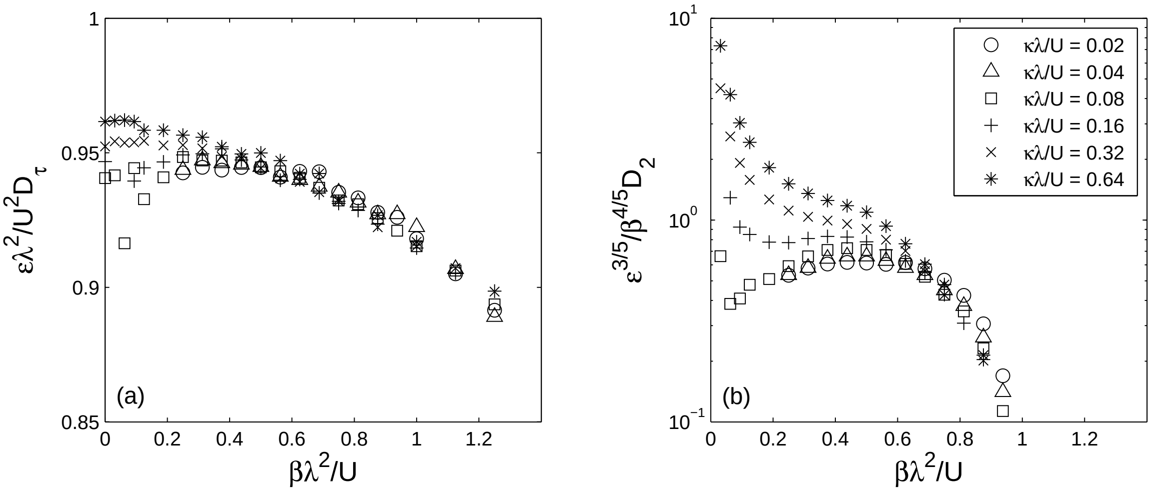

Figure 5: (*a*) Ratio of terms in the energy balance approximation $U^2 D_\tau/\lambda^2 \approx \varepsilon$. The systematic departure from 1 is because the hyperviscous dissipation is not included in definition of ε in (3). (*b*) The ratio $D_2 \propto \varepsilon^{3/5}\beta^{-4/5}$.

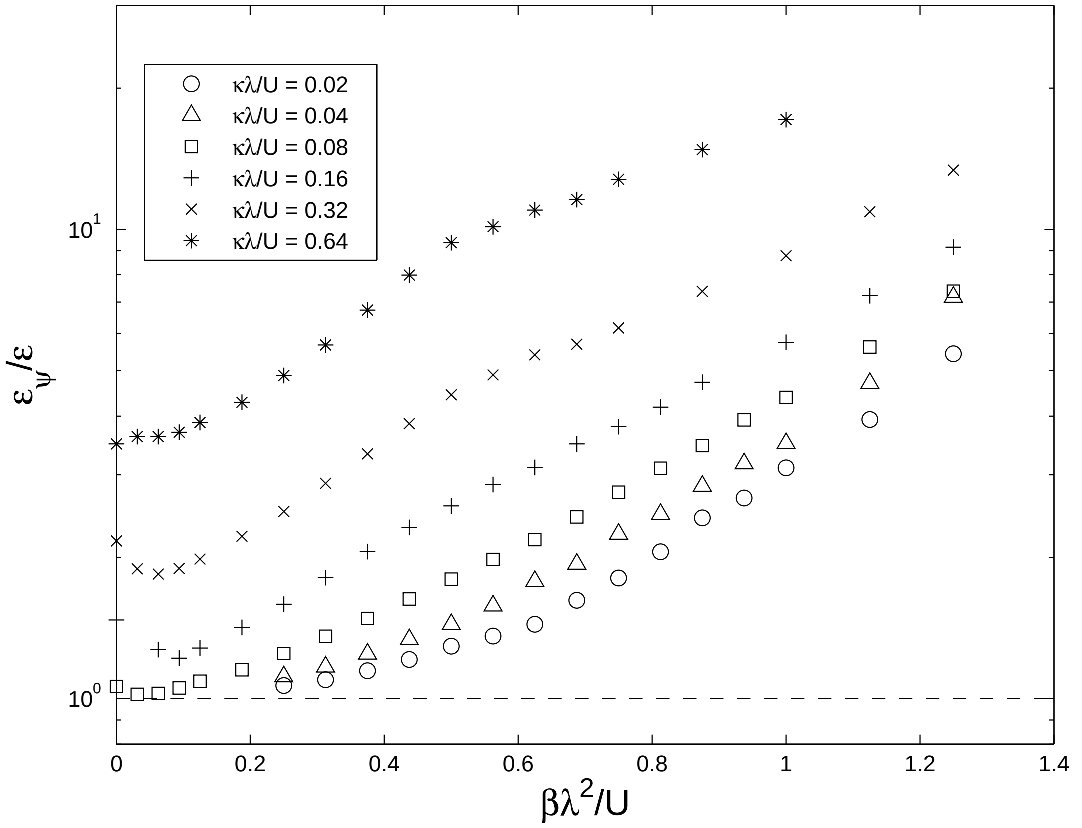

Figure 6: Ratio of the dissipation by the barotropic mode ε_ψ defined in (12) to the total dissipation ε defined in (3).

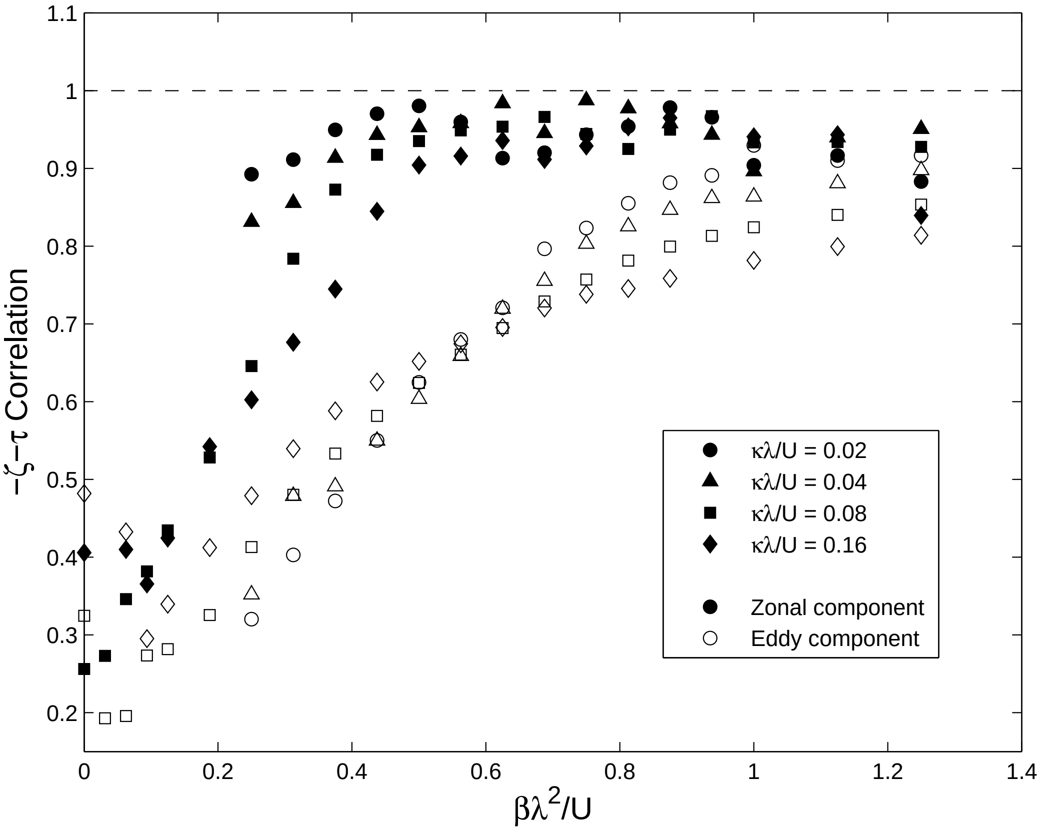

Figure 7: Negative correlation $-\langle\zeta\tau\rangle/\sqrt{\langle\zeta^2\rangle\langle\tau^2\rangle}$ between the barotropic vorticity ζ and the temperature τ for both zonally-averaged (solid symbols) and eddy (open symbols) components of the flow.

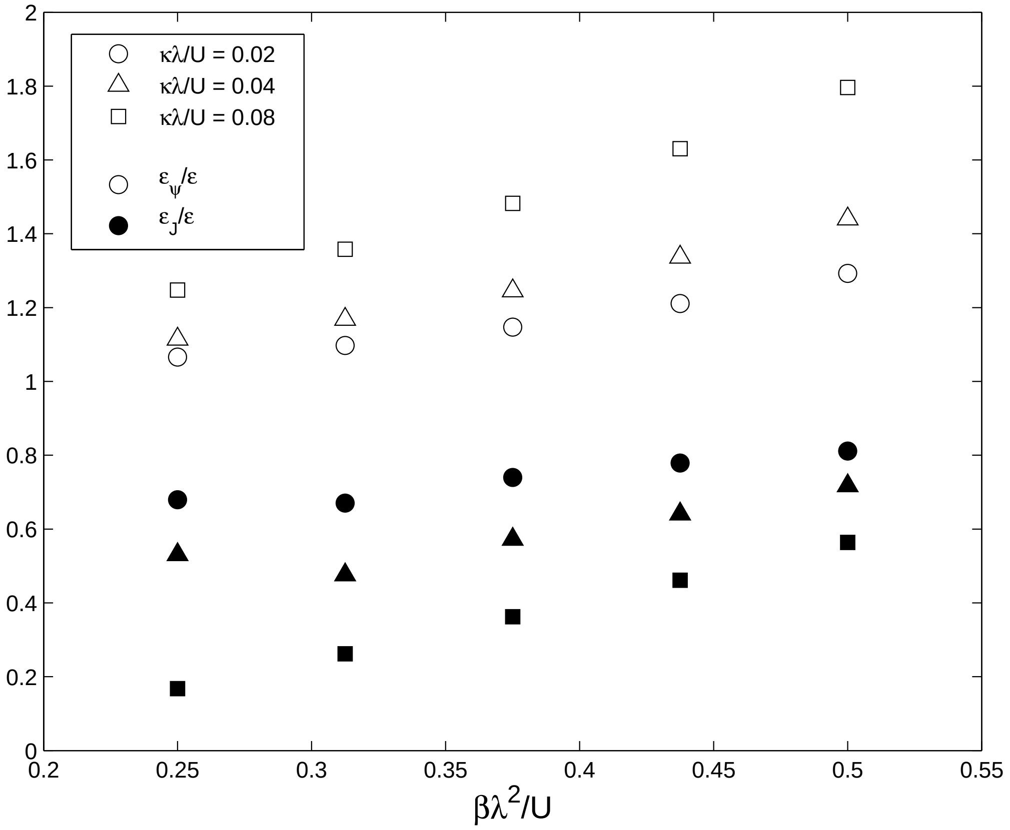

Figure 8: Open symbols show $\varepsilon_\psi/\varepsilon$ for the 15 runs which come close to satisfying $\varepsilon_\psi/\varepsilon \approx 1$. The closed symbols show $\varepsilon_{\rm J}/\varepsilon$ where $\varepsilon_{\rm J} \equiv \kappa u_{\rm J}^2$ is the dissipation in the zonal mean flow.

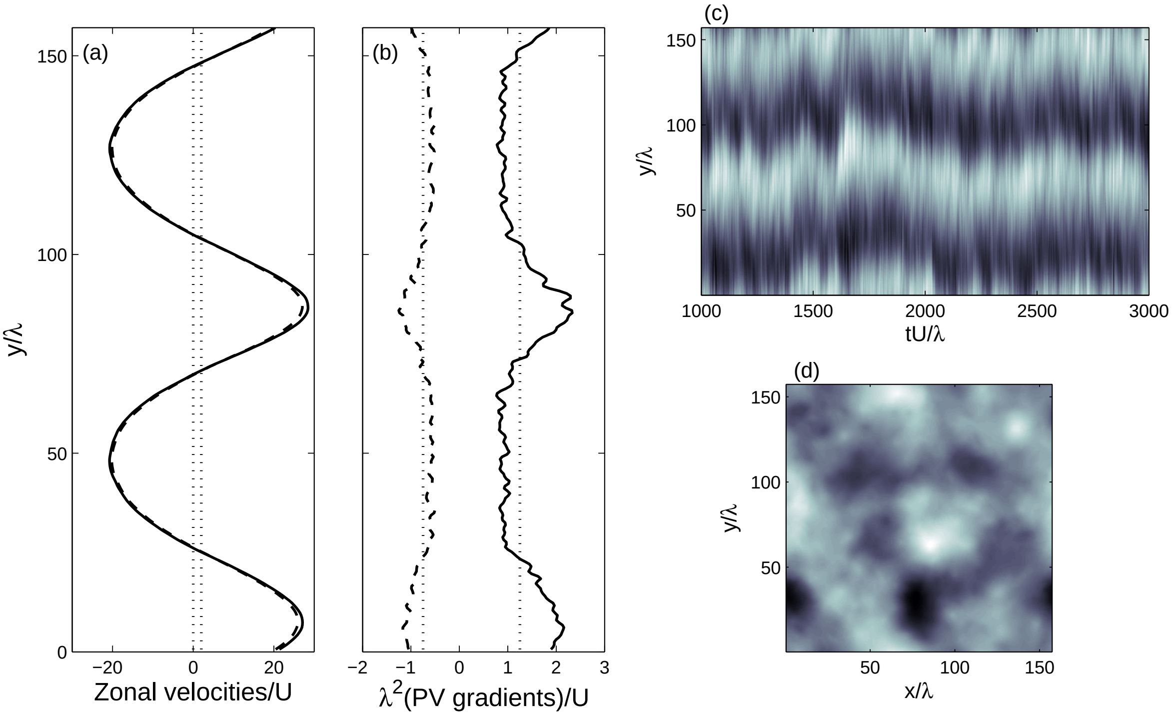

Figure 9: The run with $\kappa_* = 0.04$ and $\beta = 0.25$. (*a*) Upper (solid) and lower (dashed) zonal mean velocities; the zonal mean flow is almost barotropic and much faster than the basic state velocity jump $2U$ which is indicated by the dotted lines. (*b*) The zonal mean PV gradients upper (solid) and lower (dashed) layers. (*c*) A Hovmoller plot showing the meandering of the zonal jets. (*d*) A snapshot of the barotropic eddy streamfunction ψ'.

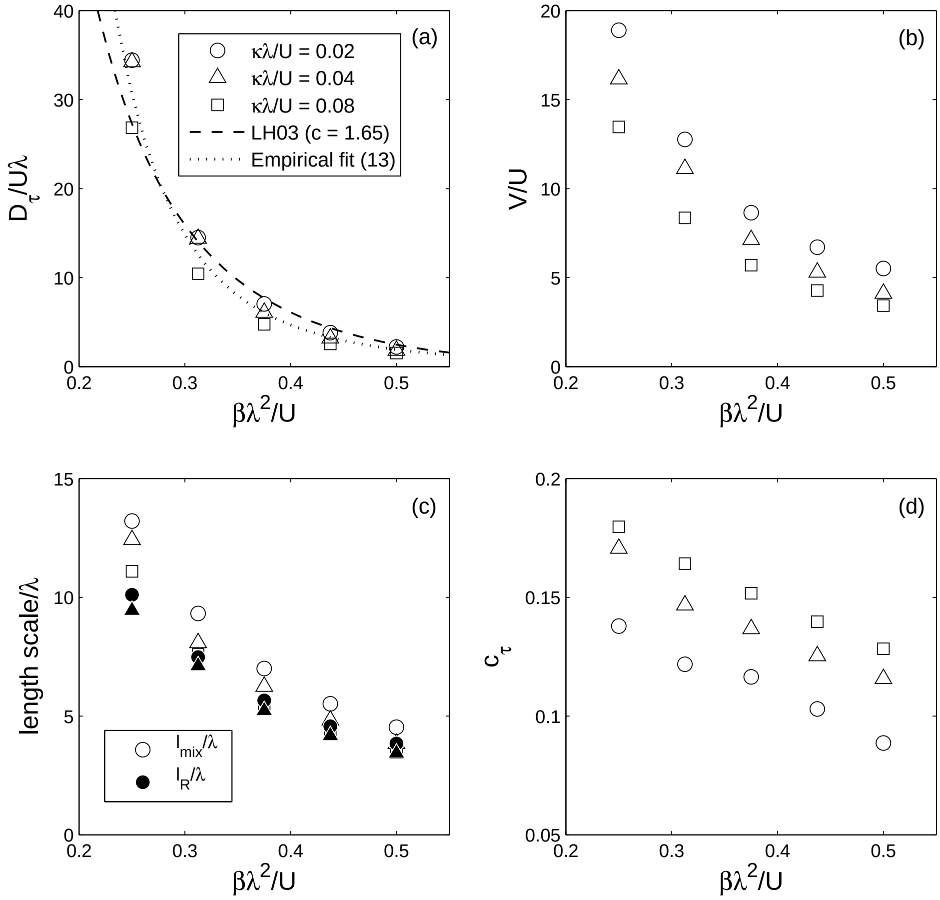

Figure 10: (*a*) An expanded view of the eddy diffusivity for the 15 runs defined by (18). The dashed curve is the LH03 parameterization (11) and the dotted curve is the empirical fit $0.12\beta_*^{-4}$. The open symbols in panels (*b*), (*c*) and (*d*) show the statistics defined in (19) through (21). The filled symbols in panel (*c*) show the Rhines scale ℓ_R as defined in (33).

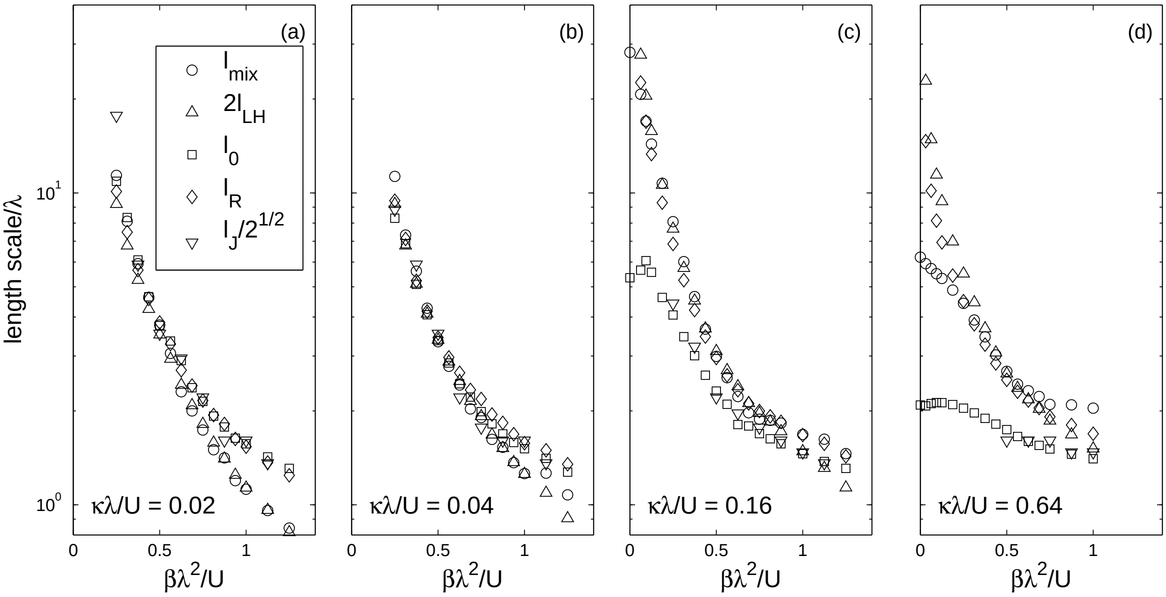

Figure 11: Eddy length scales $\ell_{\rm mix}$ (20), $2\ell_{\rm LH}$ (31), ℓ_0 (32), $\ell_{\rm R}$ (33) and $\ell_{\rm J}/\sqrt{2}$ (25) as a function of $\beta\lambda^2/U$ at four different values of $\kappa\lambda/U$. We use $2\ell_{\rm LH}$ to give good agreement with the other length scales. In panels (*a*) and (*b*) the five lengths converge to a common value as κ_* and β_* decrease.

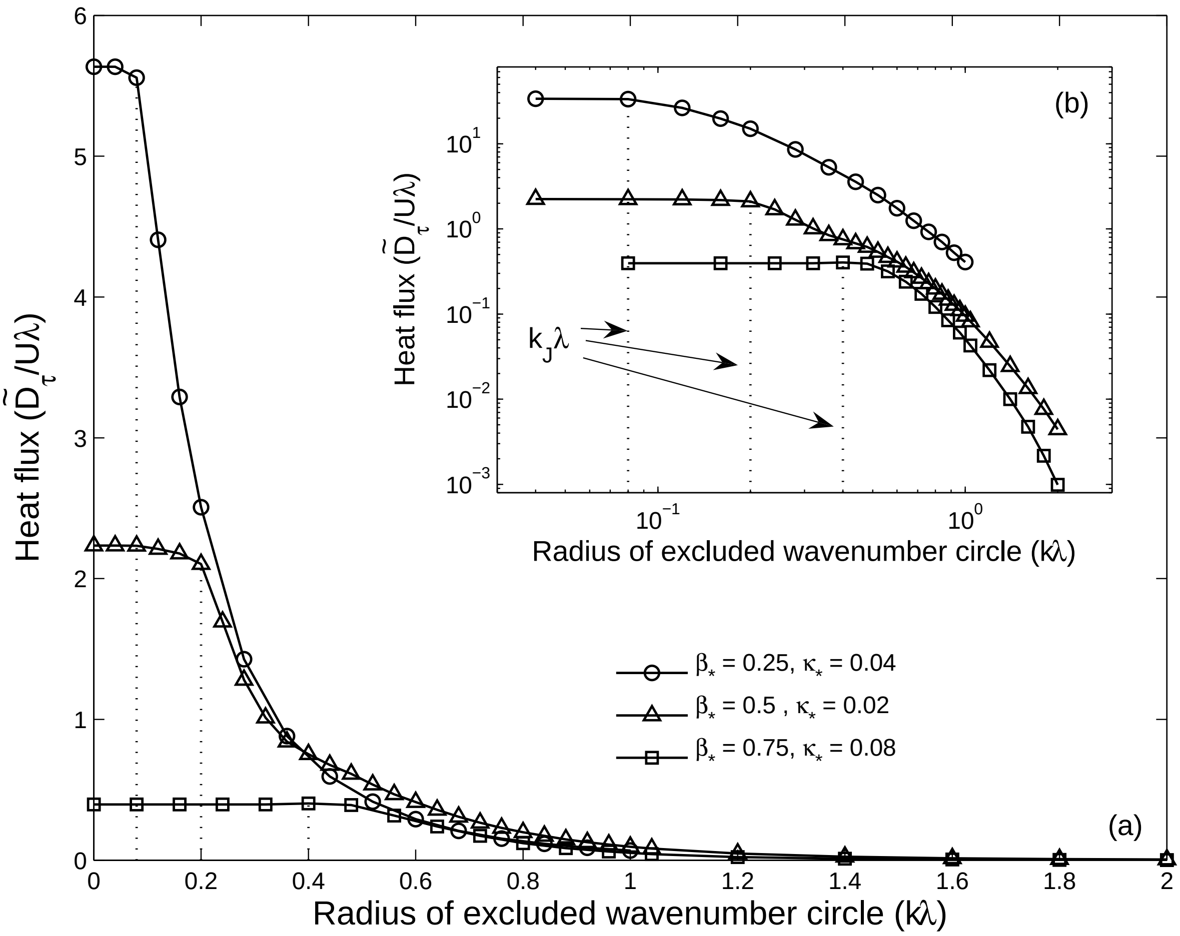

Figure 12: (*a*) The truncated eddy heat flux $\tilde{D}_\tau/U\lambda$ as a function of the radius of the excluded wavenumber circle R for three simulations. Truncated fields $\tilde{\psi}$ and $\tilde{\tau}$ are formed by setting Fourier coefficients for wavenumbers less than R equal to zero. The time and spatial average $\left\langle \tilde{\psi}_x \tilde{\tau} \right\rangle$ is $U^2\lambda^{-2}\tilde{D}_\tau$; for the $\circ$'s, $\tilde{D}_\tau$ is divided by a factor of 6. The jet wavenumber $k_J\lambda$ for each simulation is given by the dotted lines. (*b*) The same data as in panel (*a*) shown on log-log axes.

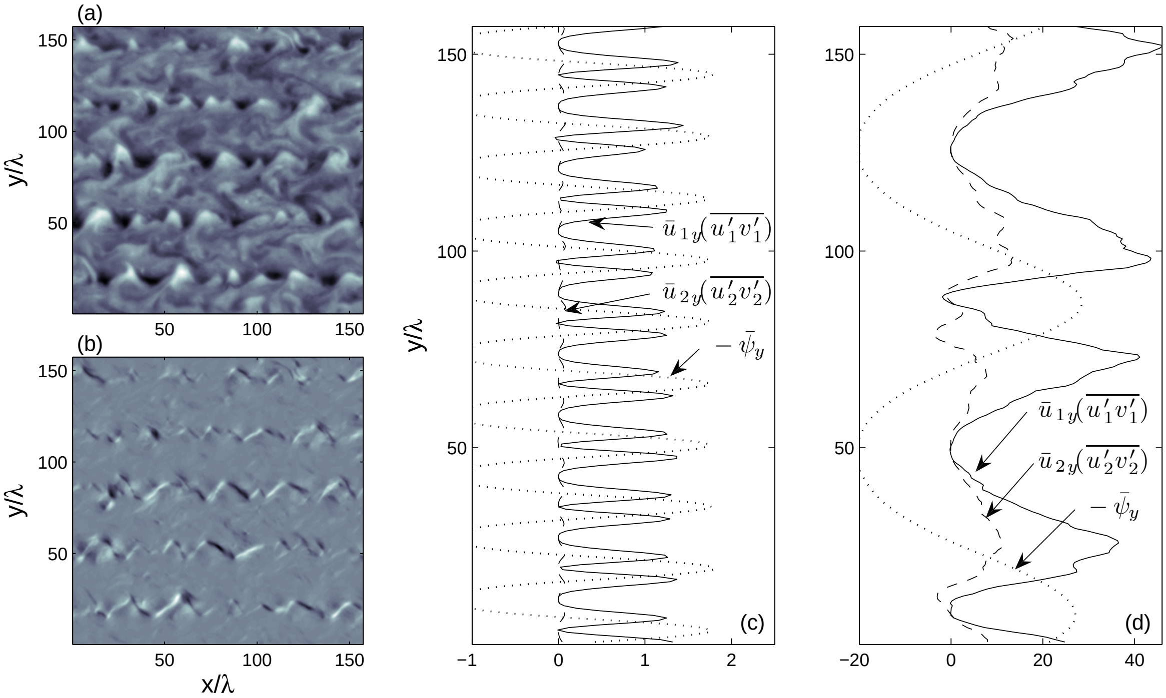

Figure 13: (*a*) Snapshot of the eddy temperature field (baroclinic streamfunction) $\tau' = \tau - \bar{\tau}$ for the simulation $\beta_* = 0.5$ and $\kappa_* = 0.02$. The baroclinic field is less isotropic than its barotropic counterpart in Figure 1(*d*). (*b*) Snapshot of the upper layer Reynolds stresses $u_1'v_1'$ for the same simulation. (*c*) Zonal and time averages of the energy transfer terms in upper (solid line) and lower (dashed line) layers for the simulation $\beta_* = 0.75$ and $\kappa_* = 0.08$. The barotropic zonal velocity divided by a factor of 2 is given by the dotted line. (*d*) Same as panel (*c*) for the simulation $\beta_* = 0.25$ and $\kappa_* = 0.02$. These curves are noisier because the jets are less steady (Figure 9). Note *upper layer* eddy shearing on the jet flanks plays an important role in energizing the zonal mean flow.

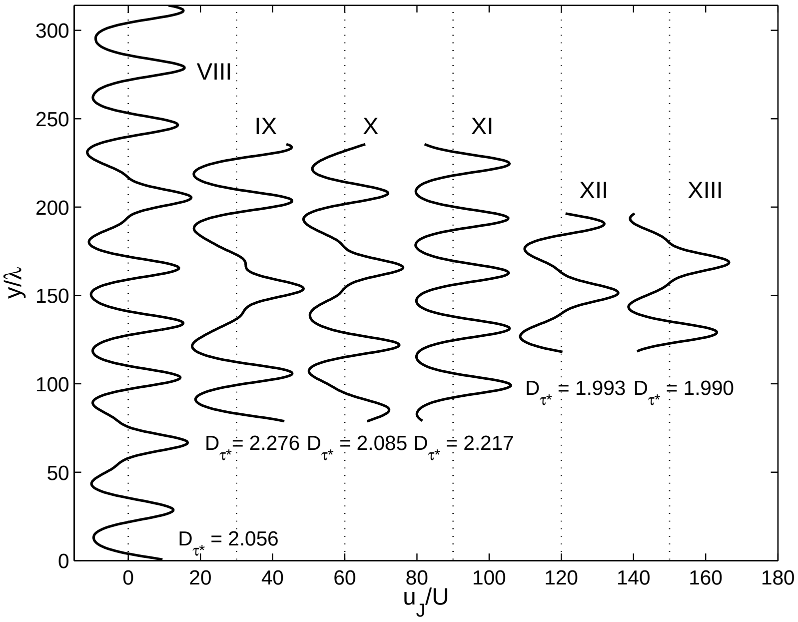

Figure 14: Zonal and time-averaged barotropic velocities $u_J(y) \equiv -\bar{\psi}_y$ for sensitivity studies (VIII-XIII) listed in Table 1 with $\beta_* = 0.5$. For clarity the curves have been translated horizontally; intersections with the dotted lines indicate zero crossings u_J. The five runs correspond to varying domain sizes and resolutions. Most runs suffer from quantization problems that may be related to differences in the hyperviscosity parameter. Run XI is stable and has an odd number of jets, therefore a quantization problem may be expected when halving the domain size (Runs XII and XIII). The domain-averaged heat flux is indicated for each simulation; domain-averaged statistics are within ±5% for all runs with $\beta_* > 0.25$ (see Table 1).